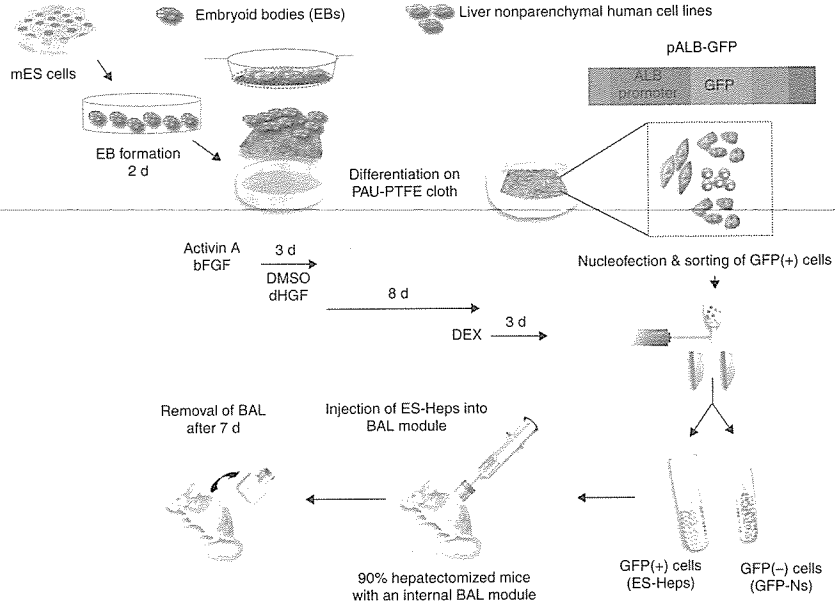

Figure 1 Schematic representation of the strategy for differentiation of mouse embryonic stem cells to hepatocytes and their use for BAL therapy. Mouse embryonic stem cells (mES cells) were cultured in suspension method for 2 d to form embryoid bodies (EBs). The resulting embryoid bodies were transferred onto unwoven polytetrafluoroethylene (PTFE) cloth and treated with fibroblast growth factor (FGF)-2 (100 ng/ml) and activin A (100 ng/ml) for 3 d, then cocultured with MMC-C-treated human nonparenchymal liver cell lines on Matrigel-layered trans-well membranes, with the deleted variant of hepatocyte growth factor (dHGF; 100 ng/ml) and 1% dimethyl sulfoxide (DMSO) for 8 d, and at the end stage with dexamethasone (DEX; 10^{-7} M) for 3 d. Finally, the cells were transduced with a plasmid containing green fluorescent protein (GFP) cDNA under the control of the albumin promoter (pALB-GFP). The GFP^+ cells (ES-Heps) were used to inoculate a BAL module implanted into 90% hepatectomized mice. The GFP^- cells served as a negative control.

mice with acute liver failure, which uniformly die within 4 d of inducing hepatic failure, resulted in 90% long-term animal survival.

RESULTS

Differentiation of mouse ES cells into hepatocytes

To induce differentiation of mouse ES cells toward hepatocytes, we first generated embryoid bodies by growing the cells in suspension culture for 2 d. The embryoid bodies were transferred to a flask containing a poly-amino-urethane (PAU)-coated, nonwoven polytetrafluoroethylene (PTFE) fabric that allows cell adhesion, and cells were cultured for 3 d in the presence of FGF-2 and human activin A. Cells were then cultured in the presence of mitomycin-C (MMC-C)–treated conditionally immortalized human liver nonparenchymal cells. Cells cocultured in this way were treated for 8 d in DMSO and dHGF and then cultured for 3 d in dexamethasone (**Fig. 1**).

Gene expression profile of mouse ES cell–derived hepatocytes

To determine the time course and degree to which ES cells were induced to differentiate into hepatocytes, we used reverse-transcriptase (RT)-PCR at various times during the culture process

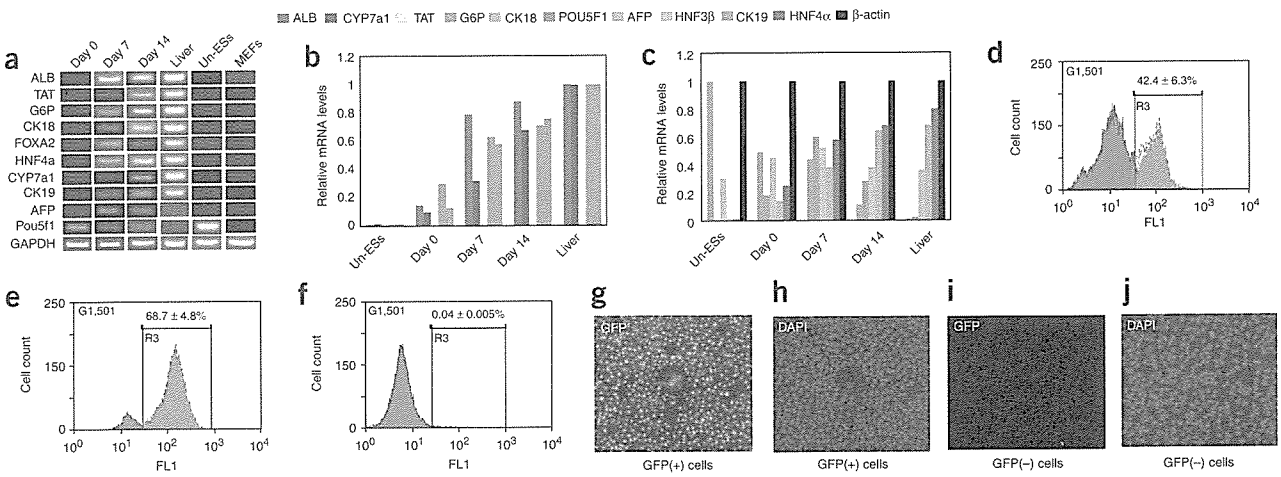

Figure 2 Characterization and purification of mouse ES cell-derived hepatocytes. (**a**) At 0, 7 and 14 d during the process of differentiating mES cells into hepatocytes, the expression of lineage-specific hepatic markers (ALB, TAT, G6P, CK18, CK19, and CYP7A1), endoderm markers (HNF-3 β, HNF-4 α and AFP) and a marker for undifferentiated cells (Pou5f1) were analyzed by RT-PCR. Mouse liver (Liver) served as the positive control, and undifferentiated mouse ES cells (Un-ESs) and mouse embryonic fibroblasts (MEFs) served as negative controls. (**b**,**c**) Expression profiles were confirmed by real-time RT-PCR analysis, and mRNA expression levels were normalized relative to beta-actin and normal adult mouse liver. (**d**–**f**) After 14 d of differentiation culture with growth factors alone (**d**) or with coculture using non-parenchymal cells (**e**), cells were transfected with pALB-GFP and analyzed by FACS. (**f**) Un-ESs transfected with pALB-GFP served as a control. (**g**,**h**) After MoFlo sorting, 100% of recovered cells were GFP-positive as confirmed by Dapi nuclear staining (**h**). (**i**,**j**) GFP-negative cells recovered by MoFlo served as control for BAL therapy. Scale bar, 100 μm (**g**–**j**). The data are representative of at least three independent experiments. AFP, alpha fetoprotein; ALB, albumin; CK18, cytokeratin-18; cytokeratin-19; CYP7A1, cytochrome P450; G6P, glucose-6-phosphate; HNF-3 beta, hepatic nuclear factor-3 β; HNF-4 α, hepatic nuclear factor-4 α; TAT, tyrosine aminotransferase.

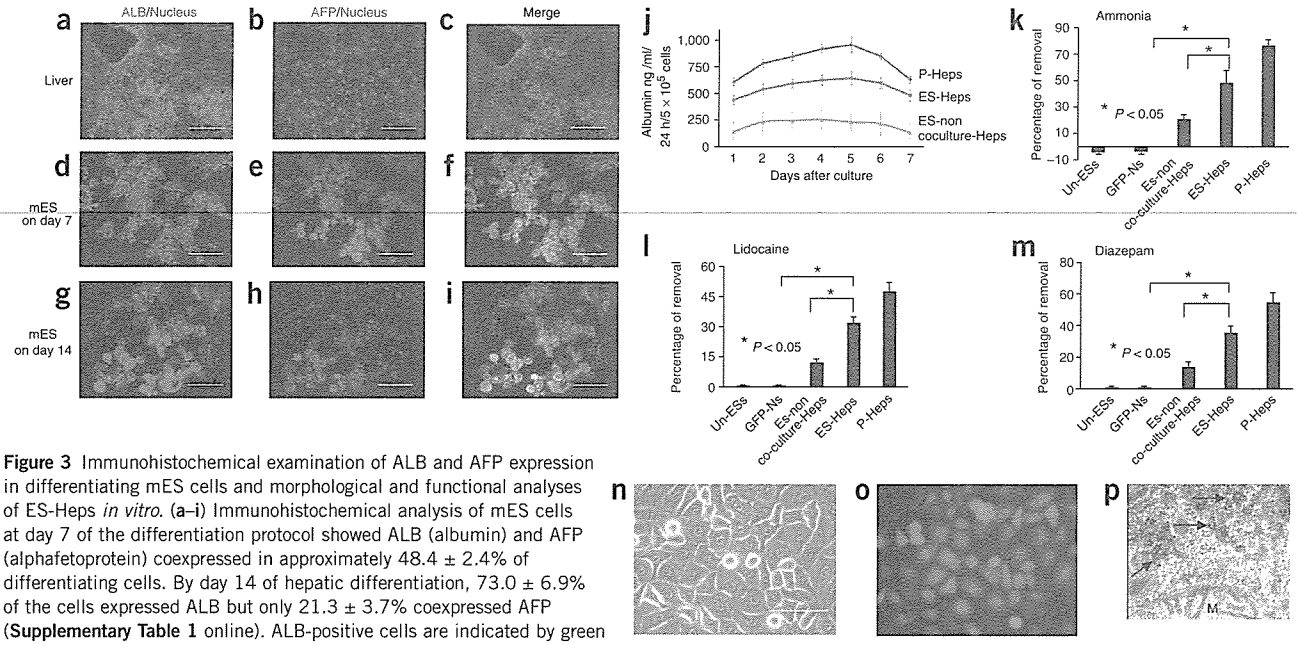

Figure 3 Immunohistochemical examination of ALB and AFP expression in differentiating mES cells and morphological and functional analyses of ES-Heps *in vitro*. (**a–i**) Immunohistochemical analysis of mES cells at day 7 of the differentiation protocol showed ALB (albumin) and AFP (alphafetoprotein) coexpressed in approximately 48.4 ± 2.4% of differentiating cells. By day 14 of hepatic differentiation, 73.0 ± 6.9% of the cells expressed ALB but only 21.3 ± 3.7% coexpressed AFP (**Supplementary Table 1** online). ALB-positive cells are indicated by green fluorescence staining; AFP-positive cells are indicated by red fluorescence staining; nuclei are stained with DAPI blue. Mouse adult liver was used as control. Scale bar, 50 μm. (**j**) Albumin secretion by ES-Heps and mouse primary hepatocytes (P-Heps) was measured ($n = 5$). (**k,l,m**) We loaded ammonium sulfate (0.56 mM), lidocaine (100 mg/ml) (**l**) or diazepam (100 μg/ml) (**m**) into culture wells containing ES-Heps (5×10^5 cells). The amount remaining was measured 24 h later and the amount metabolized was calculated per mg cellular protein. (**n,o**) Light microscopy showed that ES-Heps were morphologically polygonal with enriched cytoplasmic granules (**n**) and immuno-positive for albumin (**o**). (**p**) Transmission electron microscopy showed accumulation of glycogen rosettes in ES-Heps (arrows). (**n–p**) Scale bar, 50 μm. (**p**) Original magnification × 30,000. Undifferentiated mouse embryonic stem cells (Un-ESs) and GFP-negative cells (GFP-Ns) were negative controls, and P-Heps was a positive control ($n = 5$).

to analyze markers for endoderm-specific gene expression (alpha fetoprotein (*Afp*), hepatocyte nuclear factor (*Foxa1*)-3 β and *HNF-4α*); hepatocyte-specific gene expression (albumin (*Alb1*), tyrosine-aminotransferase (*Tat*), glucose-6-phosphate (*G6pc*), cytokeratin 18 (*Krt18*), cytokeratin-19 (*Krt19*) and cytochrome P450 (*Cyp7a1*)); and for undifferentiated ES cells (*Pou5f1*). Hepatocyte-specific gene expression occurred within 7 d and increased by day 14 of differentiation, although the level of expression was somewhat lower than that of normal hepatocytes. Endoderm-specific gene expression was also increased. *Pou5f1* expression gradually decreased during culture with growth factors and feeder cells (**Fig. 2a–c**), confirming progressive differentiation toward hepatocytes in a population of cells, and *Afp* expression, which is present in endoderm but is not expressed by mature hepatocytes, was still detected 14 d after differentiation culture, indicating that differentiation toward a mature hepatocyte phenotype was not uniform.

Cells were further analyzed by RT-PCR to determine whether differentiation was liver specific (**Supplementary Methods** online). From day 0 to 7 of the differentiation program, mouse ES cells expressed genes specifically associated with definitive endoderm (*Gsc*, *Cdh3* and *Sox17*) and transiently expressed the primitive streak gene, brachyury, indicating induction of mesendoderm. Genes indicating differentiation toward ectoderm (*Ache* and *Pax6*) and mesoderm (*Nkx2.5* and *Gata-4*), a gene specific for pulmonary differentiation (*Spc*), pancreatic marker genes (*Ipf1* and *Neud4*) and a common hepatic-pancreatic transcription factor (*Onecut1*, formerly known as *HNF-6*) were also analyzed. None of the ectoderm, pulmonary or pancreatic marker genes was expressed in differentiating mES cells after day 7, but *Gata-4* and *Onecut1* expression was induced and maintained until the end of the differentiation program (day 14), indicating development of endoderm-derived cells including common hepatic-pancreatic precursors (**Supplementary Fig. 1** online).

Immunohistochemical staining of ES cell–derived hepatocytes (ES-Heps) showed that 48.4 ± 2.4% of mouse ES cells coexpressed albumin (ALB) and AFP on day 7 of the differentiation protocol. By day 14, 73.0 ± 6.9% of ES cell–derived cells expressed ALB, but only 21.3 ± 3.7% coexpressed AFP (**Supplementary Table 1** online).

Coculture enhances differentiation of ES cells

To select ES cells that differentiated toward hepatocytes, we transfected embryoid body–derived cells with a plasmid vector containing the gene encoding green fluorescent protein (GFP) under the control of the albumin promoter (pALB-GFP). After transfection, embryoid body–derived cells expressing albumin would also express GFP. GFP expression was strongly affected by culture conditions. When embryoid body cells were cultured with growth factors only (without cell coculture), 42.4 ± 6.3% of cells actively expressed GFP and thus transcribed albumin. When embryoid body cells were cultured on conditionally immortalized human stellate cells, endothelial cells and cholangiocytes, the percentage of GFP-expressing cells increased to 68.7 ± 4.8% (**Fig. 2d–f**).

Characteristics of flow-sorted, albumin-expressing ES-Heps

Albumin-expressing, GFP-positive cells generated with and without cell coculture were isolated by a cell sorter MoFlo, and GFP expression was confirmed by fluorescence microscopy and Dapi nuclear staining (**Fig. 2g,h**). Incompletely differentiated, GFP-negative cells (GFP-Ns; **Fig. 2i,j**) were used as negative controls for subsequent experiments.

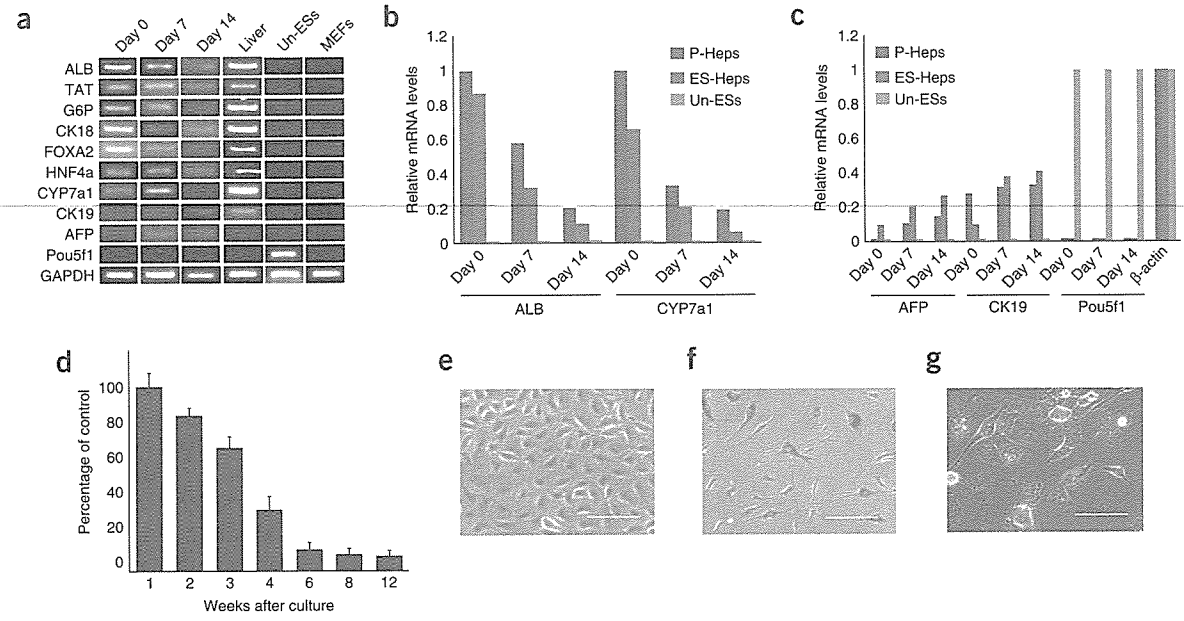

Figure 4 Fate of ES-Heps in long-term culture. ES-Heps were differentiated from mES cells and cultured under standard hepatocyte culture conditions for 12 weeks. (**a**) The expression of lineage-specific hepatic markers (ALB, TAT, G6P, CK18, CK19, and CYP7A1), endoderm markers (HNF-3 β, HNF-4 α, and AFP) and a marker for undifferentiated cells (Pou5f1) was analyzed by RT-PCR. (**b**,**c**) Expression profiles were confirmed by real-time PCR analysis, and mRNA expression levels were normalized relative to GAPDH. (**d**) ES-Heps (1×10^6) were inoculated into 6-well plates and the cell number of cultured ES-Heps was calculated weekly by trypan blue exclusion for 12 weeks. (**e–g**) ES-Heps were subjected to senescence-associated β-galactosidase staining after (**e**) 1 week and (**f**) 6 weeks of culture and (**g**) photographed under phase contrast after 6 weeks of culture. The data are representative of at least three independent experiments. AFP, alpha fetoprotein; ALB, albumin; CK18, cytokeratin-18; cytokeratin-19; CYP7A1, cytochrome P450; G6P, glucose-6-phosphate; HNF-3 beta, hepatic nuclear factor-3 β; HNF-4 α, hepatic nuclear factor-4 α; TAT, tyrosine aminotransferase.

ES-Heps secreted albumin at 300–600 ng/ml/24 h/5 × 10^5 cells, ~70% of that produced by primary mouse hepatocytes, and metabolized 49 ± 8.5% of loaded ammonia, 32.3 ± 2.8% of lidocaine and 35.6 ± 4.7% of diazepam. ES-Heps derived without coculture with liver nonparenchymal cells (ES-non coculture-Heps) secreted albumin at 150–250 ng/ml/24 h/5 × 10^5 cells, ~20% of that produced by primary mouse hepatocytes, and metabolized only 21.3 ± 3.0% of loaded ammonia, 12.3 ± 1.5% of lidocaine and 14.6 ± 3.0% of diazepam. GFP-Ns and undifferentiated mouse ES cells produced no albumin and did not metabolize any of the above compounds (**Fig. 3j–m**).

We also examined the relative contribution of each cell line to the differentiation process. Coculture with liver endothelial (TMNK-1) cells was superior for generating albumin-promoter-derived GFP-positive cells and improved cell function better than coculture with the other two cell lines. Coculture of ES cells with all three cell lines maximized the differentiation process toward functional hepatocytes (**Supplementary Fig. 2** online).

Under light microscopy, ES-Heps were polygonal in shape, contained cytoplasmic granules (**Fig. 3n**) and uniformly expressed albumin (**Fig. 3o**). Transmission electron microscopy revealed glycogen granules (**Fig. 3p**), further suggesting that GFP-positive cells were hepatocytes. Hepatocyte-specific gene expression was enriched in MoFlo-sorted GFP-positive ES-Heps but expression diminished over time, as did the number of ES-Heps surviving in culture (**Fig. 4**). Expression of senescence-associated β-galactosidase by ES-Heps began to appear after 6 weeks in culture, indicating that ES-Heps, like primary mouse hepatocytes, become senescent in culture. We also determined whether ES-Heps produce undesirable secreted proteins or proteins representing differentiation toward a nonhepatic phenotype. ES-Heps produced no proteases in culture and did not express gastrin, secretin or amylase (**Supplementary Fig. 3** online). Finally, transplantation of 1 × 10^6 ES-Heps into the subcutaneous tissue of severe combined immune deficiency (SCID) mice (n=10) generated no tumors over a 6-month observation period, whereas transplantation of 1 × 10^6 undifferentiated mouse ES-cells generated tumors 30–35 mm in diameter within 6 weeks of implantation.

Use of an ES-Hep–containing BAL in liver failure

To determine whether ES-Heps could correct a physiologically significant deficiency in hepatic function, we employed the 90% hepatectomy model of acute liver failure in mice, which produces hyperammonemia-induced hepatic encephalopathy, hypoglycemia and 100% mortality in animals within 4 d of hepatectomy. A liver assist device module consisting of a PAU-coated PTFE ethylene vinylalcohol copolymer (EVAL) membrane and a polyester supporting fabric coated by gelatinized FGF-2 (**Supplementary Figs. 4–6** online) was implanted into the subcutaneous tissue at the time of hepatectomy through a 10-mm abdominal incision. A cell injection port was then fixed in the subcutaneous space. We then introduced 5 × 10^6 primary mouse hepatocytes, undifferentiated ES cells, GFP-Ns, ES-non coculture-Heps or ES-Heps, equivalent to 5% of the mouse liver mass, into the device on the day of hepatectomy and 1 and 3 d after hepatectomy to produce a BAL.

Untreated mice that underwent 90% hepatectomy became hypoglycemic, their blood ammonia levels increased substantially and they developed encephalopathy. The response to hepatectomy was unaffected

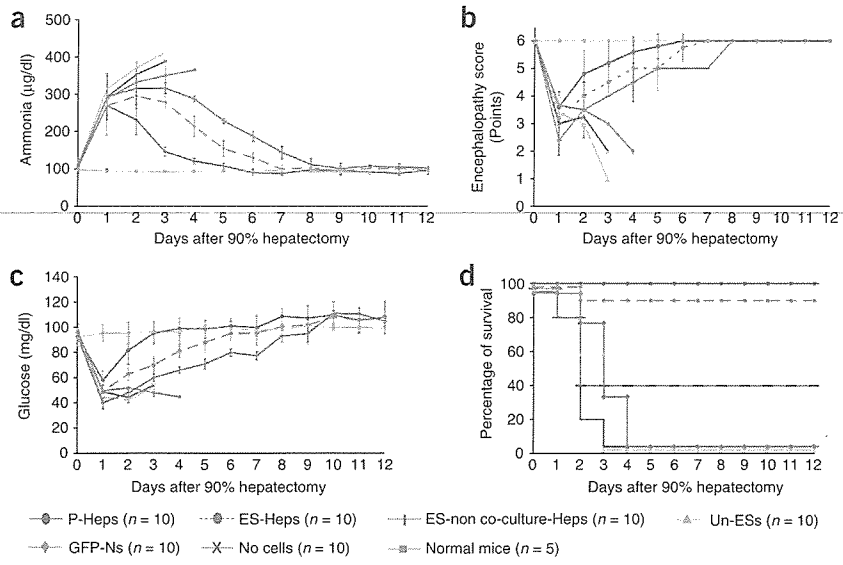

Figure 5 Ammonia, hepatic encephalopathy, blood glucose, and survival of hepatectomized mice after BAL therapy. Mice were hepatectomized (90% liver removal) and implanted with BAL modules containing primary hepatocytes (P-Heps), ES-Heps, ES-non coculture-Heps (derived under conditions where no coculture with liver non-parenchymal cells was performed), undifferentiated ES cells (Un-ESs), GFP-negative cells (GFP-Ns), or no cells. (**a**) Blood ammonia levels, (**b**) encephalopathy scores, (**c**) blood glucose levels, and (**d**) survival were determined for 12 d.

by treatment with a BAL charged with undifferentiated ES cells or GFP-Ns (**Fig. 5**). However, treatment with a BAL charged with ES-Heps caused blood glucose and ammonia levels to normalize by 6 d after induction of hepatic failure (**Fig. 5a,c**). Encephalopathy also reversed, most likely the result of correcting the blood ammonia level (**Fig. 5b**). These responses were identical to those seen after treatment with a BAL charged with primary mouse hepatocytes (**Fig. 5**). Finally, all hepatectomized mice treated with a BAL charged with undifferentiated ES cells or GFP-Ns died within 4 d of hepatectomy from acute liver failure, whereas 90% of hepatectomized mice treated with the BAL charged with ES-Heps survived (**Fig. 5d**) and had regenerated their remnant liver. Only 40% of hepatectomized mice treated with a BAL charged with ES-non coculture-Heps survived, indicating that coculture significantly enhanced hepatocyte differentiation.

Characteristics of ES-Heps following use in the BAL

ES-Heps were examined 7 d after implantation of the BAL in hepatectomized mice with liver failure. Cells had attached to the surface of the PTFE membrane of the BAL module in a trabecular pattern (**Fig. 6a,b**) and transmission electron microscopy showed the

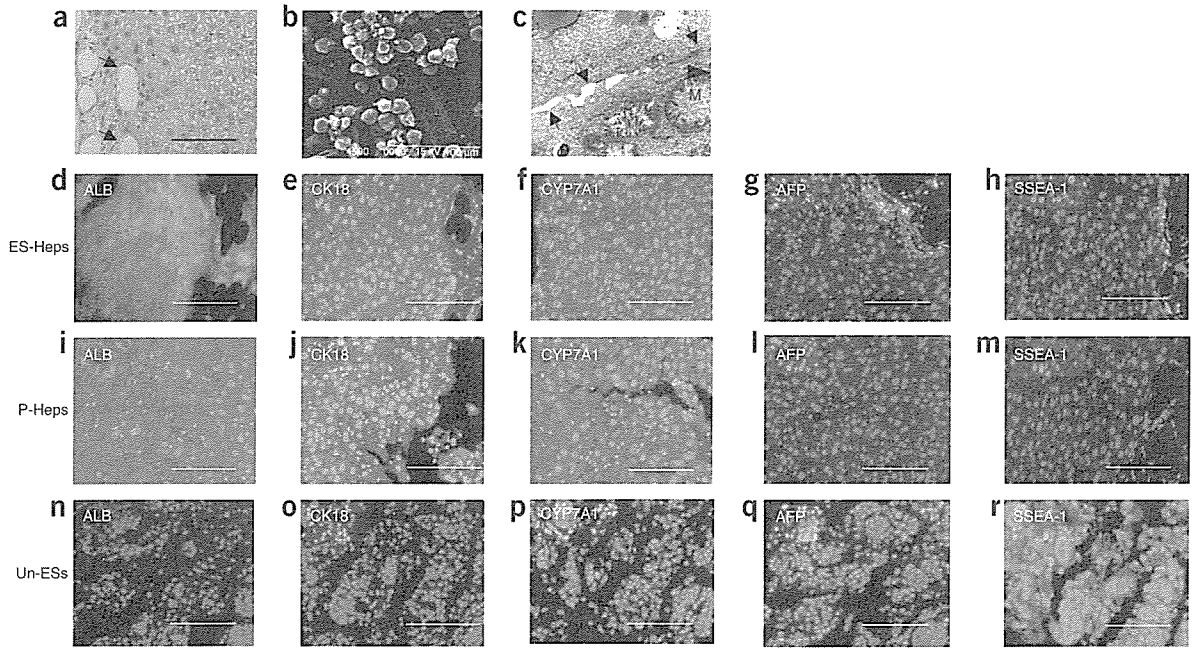

Figure 6 Morphologic and histological analysis of ES-Heps in BAL modules. Hepatectomized mice were implanted with BAL modules containing ES-Heps, primary hepatocytes (P-Heps), or undifferentiated ES cells (Un-ESs), and BAL modules were removed from surviving mice 7 d later. (**a**) HE staining showed the trabecular pattering of ES-Heps in BAL modules. Arrows indicate the PTFE cloth. (**b**) Scanning electron microscopy revealed attachment of ES-Heps on the surface of the PTFE cloth. (**c**) Transmission electron microscopy revealed the presence of bile canaliculi with apical microvilli; original magnification × 30,000. (**d–h**) ES-Heps, (**i–j**) P-Heps, and (**n–r**) Un-ESs recovered from the BAL modules were immunostained for (**d,i,n**) albumin (green), (**e,j,o**) cytokeratin-18 (CK18; red), (**f,k,p**) cytochrome P450 (CYP7A1, red), (**g,l,q**) alpha-fetoprotein (AFP, red), or (**h,m,r**) stage-specific embryonic antigen-1 (SSEA-1, red). Nuclei were counter-stained with Dapi. Bars, 100 μm.

presence of glycogen rosettes, well-developed bile canaliculi with apical microvilli, and tight junctions (**Fig. 6c**). Immunohistochemistry of BAL-attached ES-Heps showed a pattern identical to that of primary mouse hepatocytes, staining positive for albumin, cytokeratin-18 and cytochrome P450, and negative for AFP and Pou5f1 (**Fig. 6d–r**).

DISCUSSION

In these studies, we present an improved and reproducible method for generating functional hepatocytes from pluripotent ES cells and a relatively simple design for artificial liver support using ES-Heps. If successful in patients, this approach would not require intensive hemodynamic monitoring. Although methods for hepatic differentiation of ES cells have been described, none have generated cells with function adequate for clinical use[19–25] or with enough phenotypic uniformity to eliminate the risk of teratoma formation[26]. We found that ES cell differentiation into cells with the capacity to function as hepatocytes was significantly enhanced by coculturing embryoid body cells with human liver nonparenchymal cells. Other investigators have demonstrated that exposure to damaged liver tissue stimulates liver cell regeneration and can enhance homing and differentiation of stem cells to a hepatocyte phenotype[13,21]. Unfortunately, differentiation strategies using damaged liver tissues have limited clinical utility.

Our strategy involves culturing embryoid bodies with activin A and FGF-2 to enhance their differentiation to definitive endoderm as previously described[27–29]. The critical importance of growth in activin A and FGF-2 to the differentiation process is demonstrated in **Supplementary Figs. 7** and **8** online. Next, recognizing the importance of heterotopic interactions between hepatocytes and hepatic nonparenchymal cells in liver development, we cocultured the endoderm-enriched cells with growth factors known to be important for hepatic differentiation[30–33] *in trans*-well plates with MMC-C–treated conditionally immortalized human liver nonparenchymal cells to enhance differentiation toward functional hepatocytes. The human liver nonparenchymal cell lines were developed in our laboratory and provide an unlimited source of human cells for hepatic differentiation. The conditionally immortalized human cholangiocytes used for these studies (MMNK-1)[16] generate interleukin-6 and TNF-alpha, the liver endothelial cells (TMNK-1)[17] produce fibroblast growth factor (FGF)4 and vascular endothelial growth factor (VEGF), and the liver stellate cells (TWNT-1)[18] produce HGF, all factors important for liver regeneration (**Supplementary Fig. 9** and **Supplementary Table 2** online). We incorporated dHGF, which lacks a 5–amino acid sequence in the first kringle domain of HGF[34], rather than the more commonly used HGF in our differentiation process because it is less cytotoxic than HGF when used at high doses in hepatocyte culture[34] (**Supplementary Fig. 10** online) and has twice the potency of HGF in stimulating DNA synthesis by rat hepatocytes[31]. The coculture differentiation strategy induced an ~50% increase in the number of ES cells becoming albumin positive, and resulted in 68.7% of the entire cell population differentiating toward a hepatocyte phenotype. The culture substrate also strongly affected the differentiation efficiency (**Supplementary Figs. 11** and **12** online).

The relevance of the procedure outlined here to human ES cells is unknown. However, differentiation of human ES cells using the PTFE cloth, rather than Matrigel, improves production of albumin and urea and metabolism of lidocaine[35], whereas high-dose dHGF, rather than HGF, further enhances differentiation (data not shown). Thus, the approach described here appears promising for application to human ES cells. However, cell sorting, as carried out here, may not be practical for isolating the billions of human ES cell–derived hepatocytes that would be needed to generate a clinically useful BAL, although simultaneous use of several MoFlo machines could reduce the time required to a few hours. Alternatively, more rapid magnetic cell sorting, using asialoglycoprotein receptor (ASGPR)-mediated positive selection or undifferentiated marker-mediated negative selection could be used. If human ES cells could reliably be differentiated to functional human hepatocytes, efficient sorting techniques will need to be developed further.

To isolate ES-Heps, we used a plasmid vector expressing GFP from an albumin promoter. This approach generated high lineage-specific GFP expression by transient high copy number transfection and avoided the difficult step of producing ES cell lines that stably express exogenous genes. Creation of stable ES cell transfectants is especially difficult to accomplish with human ES cell lines that tolerate individual cell cloning poorly. The flow-sorted, albumin-positive cells functioned *in vitro* with two-thirds the capacity of primary mouse hepatocytes.

The design of the BAL eliminates the need for vascular connection to the patient, which produces circulatory instability and requires anticoagulation in patients with liver failure who are already at high risk for bleeding from low platelet counts and coagulation factor deficiencies. The BAL module consisted of an EVAL 30-nm pore size membrane that allows free exchange of glucose and ammonia and prevents the passage of lymphocytes from the host into the device and of the cells from the device into the host, further reducing the risk of teratoma formation. Attachment of the introduced cells was facilitated by the PAU-coated PFTE cloth, which also allowed the cells to engraft in a three-dimensional structure. The BAL was coated with FGF-2 to facilitate rapid vascularization around the module surface[36] where engrafted cells remained viable for up to 16 weeks (data not shown), longer than previously reported[37,38]. Finally, the cell injection port allows repeated inoculation of the BAL with fresh cells to facilitate maintenance of a functional hepatocyte mass. Use of this device in mice with acute liver failure, which uniformly die within 4 d of inducing hepatic failure, resulted in 90% animal survival.

In summary, these mouse studies provide a foundation for differentiation of functional hepatocytes from human ES cells and a practical design for a clinically useful liver-assist device. Further studies will be needed to determine whether these methods can be adapted for use in patients.

METHODS

Animal experiments. Female Balb/c SCID mice (Nippon CLEA) were used for all transplantation procedures. Balb/c mice (Nippon CLEA) were used for hepatocyte isolation. All procedures performed on the animals were approved by the Okayama University Institutional Animal Care and Use Committee, and thus within the guidelines for humane care of laboratory animals.

Differentiation and purification of mES cells in culture. Mouse ES cells derived from Balb/c × 129sv embryos were expanded on a feeder layer of mitomycin-treated mouse embryonic fibroblasts[1], seeded on 0.1% gelatin-coated plates (R-ES-006B, Dainippon Pharmaceutical Co.), and cultured in Dulbecco's Modified Eagle Medium containing 15% FBS, 1% nonessential amino acid, 1% nucleosides, 2-mercaptomethanol (110 μM), 1% penicillin/streptomycin, 1% glutamic acid, and 500 U/mL leukemia inhibitory factor (Dainippon Pharmaceutical Co.). ES cells (2.5×10^5 cells/ ml) were suspended, inoculated into ultra-low attachment chamber (Corning), and cultured for 2 d without leukemia inhibitory factor. The resulting embryoid bodies were transferred onto an unwoven PTFE cloth coated with PAU, which has cellular adhesive properties (Kuraray Medical Co.), and treated for 3 d with 100 ng/ml FGF-2 (PreproTech EC) and 100 ng/ml activin A (R & D Systems Co.) using Dulbecco's Eagle medium Nutrient Mixture F-12 (Gibco BRL), containing 1% FBS (FBS) (Gibco BRL), 4.5 mg/ml glucose, 2 μM L-glutamine, 25 μM HEPES (Gibco BRL), 3% albumin from bovine serum (Sigma), 100 U/ml penicillin,

and 100 μg/ml streptomycin (Sigma) (**Fig. 1**). The cells were then continuously cultured on the PAU-coated PTFE fabric, while the upper chamber, isolated by a 0.4 μm pore size trans-well membrane (Becton Dickinson) was seeded with 5×10^5 mitomycin C-treated (MMC; Sigma, 10 mg/ml for 2 h) conditionally immortalized human cholangiocyte cells (MMNK-1 cells[16]), 5×10^5 liver endothelial cells (TMNK-1 cells[17]) and 5×10^5 hepatic stellate cells (TWNT-1 cells[18]) in Dulbecco's Eagle medium Nutrient Mixture F-12 (Gibco BRL), containing 4.5 mg/ml glucose, 2 μM L-glutamine, 25 μM HEPES (Gibco BRL) 100 U/ml penicillin, and 100 μg/ml streptomycin (Sigma) for 8 d with 100 ng/ml dHGF, 1% dimethyl sulfoxide and 10% FBS. For the final 3 d of culture, cells were treated with 10^{-7} M dexamethasone (Sigma). The cells were trypsinized, suspended as single cells, and transfected using Nucleofector (Amaxa Biosystems), according to the manufacturer's specifications, with a plasmid vector containing green fluorescent protein cDNA under the control of the albumin promoter (pALB-GFP). GFP expression was determined using a MoFlo cell sorter (DakoCytomation Co.), the data were analyzed by Software Summit v3.1 (DakoCytomation Co.), and GFP-positive cells, referred to as ES-Heps, were recovered for further study by MoFlo. Cells that failed to express GFP, referred to as GFP-Ns, were similarly recovered and used as negative controls for some experiments.

Mouse hepatocyte isolation and culture. For use as a positive control, primary hepatocytes were isolated from Balb/c mice weighing 20 g (Nippon CLEA) using a two-step collagenase digestion method, as previously reported[39]. The yield and viability of the isolated hepatocytes were $1.0–1.5 \times 10^7$ cells per animal and >90%, respectively.

Evaluation of metabolic capacity and albumin secretion by ES-Heps. We seeded 5×10^5 primary mouse hepatocytes, undifferentiated ES cells, ES cell–derived GFP-Ns, ES-non coculture-Heps or ES-Heps into the wells of a 12-well tissue culture plate. Individual wells were coated with a PAU-treated PTFE cloth, which provided a stable three-dimensional cell matrix for cell growth[40]. Ammonium sulfate (0.56 mM), lidocaine (1 mg/ml) and diazepam (1 μg/ml) were added to individual wells 24 h later, and the amount of each substrate remaining in the medium after culture for 24 h was measured. The ammonia concentration was determined using a Fuji Dri-Chem slide (Fuji) and concentrations of lidocaine and diazepam were measured by SRL. We measured 24-h albumin secretion into the culture medium using a mouse albumin enzyme-linked immunosorbent assay (ELISA) kit and metabolic rate was calculated as previously described[34].

Gene expression analyses. Total RNA was extracted from 1×10^6 ES-Heps, GFP-Ns cells, undifferentiated mouse ES cells, mouse liver and mouse embryonic fibroblasts (1×10^6 cells) during various stages of the differentiation process, and following MoFlo isolation and culture of ES-Heps and GFP-Ns, using RNA Trizol (Invitrogen) according to the manufacturer's protocol.

RT-PCR was performed at 22°C for 10 min and then at 42°C for 20 min using 1.0 μg of RNA per reaction, to ensure that the amount of cDNA amplified was proportional to the mRNA present in the original samples as previously reported[41] using specific primers. The following specific primers were used: albumin (AJ011413): sense strand: 5′-GACAAGGAAAGCTGCCTGAC-3′, antisense strand: 5′-TTCTGCAAAGTCAGCATTGG-3′; TAT (BC025934): sense strand: 5′-ACCTTCAATCCCATCCGA -3′, antisense strand: 5′-TCCCGACTGGA TAGGTAG -3′; G6P (U00445): sense strand: 5′-CAGGACTGGTTCATCCTT-3′, antisense strand: 5′-GTTGCTGTAGTAGTCGGT-3′; CK 18 (XM356490): sense strand: 5′-CGATACAAGGCACAGATGGA-3′, antisense strand: 5′-CTT CTCCATCCTCCAGCAAG-3′; HNF3 β (UO4197): sense strand: 5′-TATT GGCTGCAGCTAAGCGG-3′, antisense strand: 5′-GACTCGGACTCAGGTGA GGT-3′; HNF4 α (NM8261) sense strand: 5′-ATTCTCCAACAGCCTGAGC-3′, antisense strand: 5′-CGTCTGTGATGTTGGCAATC-3′, CYP 7A1 (AK050260) sense strand: 5′-AGGACTTCACTCTACACC-3′, antisense strand: 5′-GCAG TCGTTACATCATCC-3′, CK 19 (M36120) sense strand: 5′-GTGCCACCATTG ACAACTCC-3′, antisense strand: 5′-AATCCACCTCCACACTGACC-3′, AFP (V00743) sense strand: 5′-CACTGCTGCAACTCTTCGTA-3′, antisense strand: 5′-CTTTGGACCCTCTTCTGTGA-3′, Pou5f1 (NM013633) sense strand: 5′-GG CGTTCTCCTTTGGAAAGGTGTTC-3′, antisense strand: 5′-CTCGAACCAC ATCCTTCTCT-3′, and glyceraldehyde-3-phosphate dehydrogenase (GAPDH) (NM001001303): sense strand: 5′-TGAAGGTCGGTGTGAACGGATTTGGC-3′, antisense strand: 5′-TGTTGGGGGCCGAGTTGGGATA-3′, After hybridization with labeled probes, the hybridized bands were detected by radiography.

The PCR products were resolved on 1% agarose gels and visualized by ethidium bromide staining. Mouse glyceraldehyde-3-phosphate dehydrogenase (GAPDH) served as an internal control for the efficiency of mRNA isolation and cDNA synthesis. Real-time RT-PCR was performed as previously described using the LightCycler instrument and aLightCycler FastStart DNA Master SYBR Green I kit (Roche Diagnostics)[41]. Briefly, 0.1 μg of total RNA from each sample was prepared for reverse transcription, and PCR was performed in a 20 μl reaction volume in triplicate using specific primers for each gene. mRNA copy numbers were calculated from serially diluted standard curves generated from a cDNA template, which represented *in vitro* samples, and bands were confirmed with gel electrophoresis. Data was analyzed using LightCycler Software (Roche Molecular Biochemicals). All expression levels were normalized to the beta-actin control. The relative expression of genes normally expressed in the liver was determined based on the mRNA level relative to that obtained from the normal adult mouse liver. The relative expression of other genes was determined based on the mRNA level relative to the beta-actin control. After hybridization with labeled probes, the hybridized bands were detected by radiography.

Electron microscopic examination. GFP-positive ES-Heps were fixed with 4% paraformaldehyde and 0.1% glutaraldehyde in 0.1 M phosphate buffer, pH 7.4 both immediately after MoFlo sorting and after 7 d of growth in the subcutaneously implanted BAL module. Electron microscopy was performed as previously described[41]. Ten different areas were randomly chosen for examination.

Measurement of cell viability and senescence. One million ES-Heps were inoculated into each well of a 24-well plate (BD Biosciences) and their growth and viability was measured by MTT assay using 0.5 mg/ml of 3- (4,5-dimethylthiazole-2-yl)-2,5-diphenyl tetrazolium bromide (MTT reagent) (Sigma), as previously described[34]. After treatment with 0.5%EDTA-trypsin (Sigma), the number of viable hepatocytes was counted using a trypan blue exclusion test and compensated for the analysis. Senescence-associated β-galactosidase staining was also performed. Briefly, ES-Heps were washed in PBS, fixed in 0.25% glutaraldehyde for 10 min on ice, and incubated at 37 °C with a fresh staining solution consisting of 1 mg/ml of 5-bromo-4-chloro-3-indolyl β-D-galactoside, 40 mM citric acid-sodium phosphate (pH 6.0), 5 mM potassium ferricyanide, 5 mM potassium ferrocyanide, 150 mM NaCl, and 2 mM MgCl2. Staining was performed as previously described[42].

Construction of the BAL module. The BAL module was constructed using a polyethylene-vinyl alcohol membrane (30 nm pore size), which inhibits passage of immune competent cells and C3 and thus provides a degree of immune isolation, and a PAU-coated PTFE non-woven fabric, which provides a substrate for cell adhesion. The 15 × 15 mm PTFE fabric was covered with an EVAL membrane and layered with a piece of polyester supporting fabric of equal size to generate an inside BAL volume of 1.125 ml. A cell injection port was then attached. To facilitate angiogenesis around the implanted module, both surface layers of the BAL module were coated with gelatinized FGF-2 before implantation[36].

Induction of acute liver failure in mice and BAL implantation. Eight week-old female Balb.SCID mice (Nippon CLEA) underwent 90% hepatectomy to induce hepatic failure[11]. Both sides of a BAL module were coated by 2 mg of gelatinized FGF-2 microspheres[36]. Directly after hepatectomy, a BAL module was implanted subcutaneously on to the abdominal wall. Twelve, 36, and 60 h after implantation, 5×10^6 mouse primary hepatocytes, ES-Heps, GFP-Ns cells, or undifferentiated mouse ES cells were introduced in 200 μl Matrigel (BD Biosciences) and 0.5 ml culture medium into the BAL module through a subcutaneously fixed cell injection port, which was designed for easy exterior access to facilitate multiple cell infusions. To prevent animal dehydration, 1 ml of saline was injected intra-abdominally into each mouse for the first 3 d after hepatectomy. Blood was collected for levels of ammonia and glucose as previously described[34,39]. Hepatic encephalopathy was measured by means of a 6 point coma scale consisting of measurements of flexion, grasping, righting,

placement, corneal and head-shaking reflexes (6 points indicating normal behavior)[39]. Vascularization around the BAL implantation site was evaluated using a laser doppler tissue blood flow imager (Advance) and quantification was determined using Laser FlowGraphy (LFG-1 version 1.0, Softcare)[43].

Histological analyses. Differentiating mouse ES cells were embedded in medium for frozen tissue (Tissue-Tek) on days 7 and 14 of differentiation. Samples were then incubated with a polyclonal rabbit anti-mouse albumin (Cedarlane) and a polyclonal rabbit anti-mouse AFP (Santa Cruz Biotech) for analysis, as outlined below. Autopsies were also performed at the time of death or sacrifice. BAL samples were fixed with 20% formalin, embedded in paraffin, and processed for staining with hematoxylin and eosin. Additional BAL samples were incubated with polyclonal rabbit anti-mouse albumin or polyclonal rabbit anti-mouse cytokeratin-18, polyclonal rabbit anti-mouse cytochrome P450, polyclonal rabbit anti-mouse AFP, or mouse monoclonal anti-stage-specific embryonic antigen-1 (SSEA-1) (Santa Cruz Biotech), followed by Cy2- or Cy3-labeled secondary antibody (Amersham Biosciences). Samples were observed under a confocal laser scanning microscope (LSM510; Carl Zeiss).

Statistical analyses. Mean values are presented with standard deviations. ANOVA was used to calculate the significance of difference in mean values. The Kaplan-Meier method was used to calculate survival, and significance was determined by the Mann-Whitney U test. A P value <0.05 was considered statistically significant.

Note: Supplementary information is available on the Nature Biotechnology website.

ACKNOWLEDGMENTS

This research was supported in part by a Grant-in-Aid for Scientific Research (B) of the Japan Society for the Promotion of Science to N.K. and National Institutes of Health grant DK48794 to I.J.F. We thank Donna B. Stolz for useful comments for the paper. We thank Ann Kyle for editorial assistance.

AUTHOR CONTRIBUTIONS

Ira J. Fox and Naoya Kobayashi had full access to all of the data in the study and take responsibility for the integrity of the data and the accuracy of the data analyses. Study concept and design, I.J.F., N.K., A.S.-G., J.L., J.-W.Y., H.-S.J., N.T. Acquisition of data, I.J.F., N.K., A.S.-G., N.T. Analysis and interpretation of data, I.J.F., N.K., A.S.-G. Drafting of the manuscript, I.J.F., N.K., A.S.-G., J.L., J.-W.Y., H.-S.J. Critical revision of the manuscript for important intellectual content, I.J.F., N.K., A.S.-G. Statistical analysis, T.O., H.N. Obtained funding, I.J.F., N.K. Administrative, technical, or material support, I.J.F., N.K., A.S.-G., N.N.-A., J.D.R.-C., H.B., T.U., Y.T., D.Z., Y.C., K.T., M.N., A.M. Study supervision, I.J.F., N.K. All authors contributed to the preparation of the report.

COMPETING INTERESTS STATEMENT

The authors declare competing financial interests (see the *Nature Biotechnology* website for details).

Published online at http://www.nature.com/naturebiotechnology/
Reprints and permissions information is available online at http://npg.nature.com/reprintsandpermissions/

1. Lee, W.M. Acute liver failure. *N. Engl. J. Med.* **329**, 1862–1872 (1993).
2. Williams, R. & Wendon, J. Indications for orthotopic liver transplantation in fulminant liver failure. *Hepatology* **20**, S5–S10 (1994).
3. Abe, T. *et al.* Study of plasma exchange for liver failure: beneficial and harmful effects. *Ther. Apher. Dial.* **8**, 180–184 (2004).
4. Rifai, K. *et al.* Prometheus–a new extracorporeal system for the treatment of liver failure. *J. Hepatol.* **39**, 984–990 (2003).
5. Sen, S. *et al.* Pathophysiological effects of albumin dialysis in acute-on-chronic liver failure: a randomized controlled study. *Liver Transpl.* **10**, 1109–1119 (2004).
6. Chen, S.C. *et al.* Treatment of severe liver failure with a bioartificial liver. *Ann. NY Acad. Sci.* **831**, 350–360 (1997).
7. Demetriou, A.A. *et al.* Prospective, randomized, multicenter, controlled trial of a bioartificial liver in treating acute liver failure. *Ann. Surg.* **239**, 660–667, discussion 667–670 (2004).
8. Nagata, H. *et al.* Treatment of cirrhosis and liver failure in rats by hepatocyte xenotransplantation. *Gastroenterology* **124**, 422–431 (2003).
9. Platt, J.L. Xenotransplanting hepatocytes: the triumph of a cup half full. *Nat. Med.* **3**, 26–27 (1997).
10. van de Kerkhove, M.P. *et al.* Evidence for Galalpha(1–3)Gal expression on primary porcine hepatocytes: implications for bioartificial liver systems. *J. Hepatol.* **42**, 541–547 (2005).
11. Kobayashi, N. *et al.* Prevention of acute liver failure in rats with reversibly immortalized human hepatocytes. *Science* **287**, 1258–1262 (2000).
12. Alison, M.R. *et al.* Hepatocytes from non-hepatic adult stem cells. *Nature* **406**, 257 (2000).
13. Jang, Y.Y., Collector, M.I., Baylin, S.B., Diehl, A.M. & Sharkis, S.J. Hematopoietic stem cells convert into liver cells within days without fusion. *Nat. Cell Biol.* **6**, 532–539 (2004).
14. Lagasse, E. *et al.* Purified hematopoietic stem cells can differentiate into hepatocytes in vivo. *Nat. Med.* **6**, 1229–1234 (2000).
15. Schwartz, R.E. *et al.* Multipotent adult progenitor cells from bone marrow differentiate into functional hepatocyte-like cells. *J. Clin. Invest.* **109**, 1291–1302 (2002).
16. Maruyama, M. *et al.* Establishment of a highly differentiated immortalized human cholangiocyte cell line with SV40T and hTERT. *Transplantation* **77**, 446–451 (2004).
17. Matsumura, T. *et al.* Establishment of an immortalized human-liver endothelial cell line with SV40T and hTERT. *Transplantation* **77**, 1357–1365 (2004).
18. Watanabe, T. *et al.* Establishment of immortalized human hepatic stellate scavenger cells to develop bioartificial livers. *Transplantation* **75**, 1873–1880 (2003).
19. Yamamoto, H. *et al.* Differentiation of embryonic stem cells into hepatocytes: biological functions and therapeutic application. *Hepatology* **37**, 983–993 (2003).
20. Rambhatla, L., Chiu, C.P., Kundu, P., Peng, Y. & Carpenter, M.K. Generation of hepatocyte-like cells from human embryonic stem cells. *Cell Transplant.* **12**, 1–11 (2003).
21. Lavon, N., Yanuka, O. & Benvenisty, N. Differentiation and isolation of hepatic-like cells from human embryonic stem cells. *Differentiation* **72**, 230–238 (2004).
22. Yamada, T. *et al.* In vitro differentiation of embryonic stem cells into hepatocyte-like cells identified by cellular uptake of indocyanine green. *Stem Cells* **20**, 146–154 (2002).
23. Teratani, T. *et al.* Direct hepatic fate specification from mouse embryonic stem cells. *Hepatology* **41**, 836–846 (2005).
24. Teramoto, K. *et al.* Teratoma formation and hepatocyte differentiation in mouse liver transplanted with mouse embryonic stem cell-derived embryoid bodies. *Transplant. Proc.* **37**, 285–286 (2005).
25. Chinzei, R. *et al.* Embryoid-body cells derived from a mouse embryonic stem cell line show differentiation into functional hepatocytes. *Hepatology* **36**, 22–29 (2002).
26. Fujikawa, T. *et al.* Teratoma formation leads to failure of treatment for type I diabetes using embryonic stem cell-derived insulin-producing cells. *Am. J. Pathol.* **166**, 1781–1791 (2005).
27. D'Amour, K.A. *et al.* Efficient differentiation of human embryonic stem cells to definitive endoderm. *Nat. Biotechnol.* **23**, 1534–1541 (2005).
28. Yasunaga, M. *et al.* Induction and monitoring of definitive and visceral endoderm differentiation of mouse ES cells. *Nat. Biotechnol.* **23**, 1542–1550 (2005).
29. Kubo, A. *et al.* Development of definitive endoderm from embryonic stem cells in culture. *Development* **131**, 1651–1662 (2004).
30. Block, G.D. *et al.* Population expansion, clonal growth, and specific differentiation patterns in primary cultures of hepatocytes induced by HGF/SF, EGF and TGF alpha in a chemically defined (HGM) medium. *J. Cell Biol.* **132**, 1133–1149 (1996).
31. Oh, S.H. *et al.* Hepatocyte growth factor induces differentiation of adult rat bone marrow cells into a hepatocyte lineage in vitro. *Biochem. Biophys. Res. Commun.* **279**, 500–504 (2000).
32. Jung, J., Zheng, M., Goldfarb, M. & Zaret, K.S. Initiation of mammalian liver development from endoderm by fibroblast growth factors. *Science* **284**, 1998–2003 (1999).
33. Serra, R. & Isom, H.C. Stimulation of DNA synthesis and protooncogene expression in primary rat hepatocytes in long-term DMSO culture. *J. Cell. Physiol.* **154**, 543–553 (1993).
34. Chen, Y. *et al.* Transplantation of human hepatocytes cultured with deleted variant of hepatocyte growth factor prolongs the survival of mice with acute liver failure. *Transplantation* **79**, 1378–1385 (2005).
35. Soto-Gutierrez, A. *et al.* Differentiation of Human Embryonic Stem Cells to Hepatocytes Using Deleted Variant of HGF and Poly-amino-urethane-coated Non-woven Polytetrafluoroethylene Fabric. *Cell Transplant.* **15**, 335–342 (2006).
36. Wang, W. *et al.* Reversal of diabetes in mice by xenotransplantation of a bioartificial pancreas in a prevascularized subcutaneous site. *Transplantation* **73**, 122–129 (2002).
37. Gomez, N. *et al.* Evidence for survival and metabolic activity of encapsulated xenogeneic hepatocytes transplanted without immunosuppression in Gunn rats. *Transplantation* **63**, 1718–1723 (1997).
38. Roger, V. *et al.* Internal bioartificial liver with xenogeneic hepatocytes prevents death from acute liver failure: an experimental study. *Ann. Surg.* **228**, 1–7 (1998).
39. Kobayashi, N. *et al.* Hepatocyte transplantation in rats with decompensated cirrhosis. *Hepatology* **31**, 851–857 (2000).
40. Ikeda, H. *et al.* Perfect control of blood glucose in totally pancreatectomized diabetic pigs using a newly developed bioartificial pancreas. *Tissue Eng.* (in the press) (2006).
41. Narushima, M. *et al.* A human beta-cell line for transplantation therapy to control type 1 diabetes. *Nat. Biotechnol.* **23**, 1274–1282 (2005).
42. Noguchi, H. *et al.* Controlled expansion of human endothelial cell populations by Cre-loxP-based reversible immortalization. *Hum. Gene Ther.* **13**, 321–334 (2002).
43. Rafael, E., Gazelius, B., Wu, G.S. & Tibell, A. Longitudinal studies on the microcirculation around the TheraCyte immunoisolation device, using the laser Doppler technique. *Cell Transplant.* **9**, 107–113 (2000).

The Laryngoscope
Lippincott Williams & Wilkins, Inc.

Cochlear Protection by Local Insulin-Like Growth Factor-1 Application Using Biodegradable Hydrogel

Koji Iwai, MD; Takayuki Nakagawa, MD, PhD; Tsuyoshi Endo, MD; Yoshinori Matsuoka; Tomoko Kita, PhD; Tae-Soo Kim, MD, PhD; Yasuhiko Tabata, PhD; Juichi Ito, MD, PhD

Objective: **The aim of this experimental study was to examine the potential of local recombinant human insulin-like growth factor-1 (rhIGF-1) application through a biodegradable hydrogel for the treatment of cochleae.** ***Methods:*** **A hydrogel immersed with rhIGF-1 was placed on the round window membrane of Sprague-Dawley rats while a hydrogel immersed with physiological saline was applied to control animals. On day 3 after drug application, the animals were exposed to white noise at 120 dB sound pressure level (SPL) for 2 hours. Cochlear function was monitored using measurements of auditory brain stem responses (ABRs) at frequencies of 8, 16, and 32 kHz. The temporal bones were collected 7 or 30 days after noise exposure and the loss of hair cells was quantitatively analyzed.** ***Results:*** **Local rhIGF-1 treatment significantly reduced the elevation of ABR thresholds on days 7 and 30 after noise exposure. Histologic analysis revealed that local rhIGF-1 treatment significantly prohibited the loss of outer hair cells.** ***Conclusions:*** **These findings demonstrate that local IGF-1 application through the biodegradable hydrogel has the potential for protection of cochleae from noise trauma.** ***Key Words:*** **Drug delivery, cochlea, hair cell, protection, growth factor, acoustic trauma, rat.**
Laryngoscope, **116:529–533, 2006**

INTRODUCTION

In recent years, there has been increasing interest in the treatment of inner ear disorders using the local, rather than systemic, application of therapeutic agents, because the former has fewer side effects and is more target-specific. The establishment of clinically applicable strategies for the local application of therapeutic agents should therefore open a new window for the treatment of inner ear disorders. For methods of drug delivery to be viable in clinical settings, it is crucial for the procedure to be technically undemanding and as minimally invasive as possible. Based on such a background, the use of biodegradable polymers for cochlear drug delivery has been investigated.[1–3] Biodegradable polymers, which enable the sustained release of drugs to the cochlear fluid space, can be applied through an intratympanic injection. Among biodegradable polymers, we have reported the efficacy of the biodegradable hydrogel, which is made from porcine type-I collagen, for delivery of brain-derived neurotrophic factor (BDNF) into the cochlear fluid and successful protection of spiral ganglion neurons (SGNs) from degeneration as a result of the loss of cochlear hair cells.[3]

Insulin-like growth factor-1 (IGF-1) is a mitogenic peptide that plays essential roles in the regulation of growth and development in various parts of the body, including the inner ear.[4] IGF-1 is also known to be a neuroprotective agent.[5] In addition, previous studies on the inner ear have suggested the possibility of inner ear protection by IGF-1.[6,7] Moreover, recombinant human IGF-1 (rhIGF-1) has already been approved for clinical use. Our ultimate goal is for local neurotrophin application to be clinically approved for the treatment of inner ears. In the present study, we then selected rhIGF-1 as a suitable neurotrophin for local application to the cochlea using a biodegradable hydrogel as a vehicle for drug delivery. We evaluated whether the application of rhIGF-1 in this manner was effective in protecting against noise-induced hearing loss.

From the Department of Otolaryngology–Head and Neck Surgery (K.I., T.N., T.E., Y.M., T.K., T.-S.K., J.I.), Graduate School of Medicine and the Institute for Frontier Medical Science (Y.T.), Kyoto University, Kyoto, Japan.

Editor's Note: This Manuscript was accepted for publication December 5, 2005.

This study was supported by a Grant-in-Aid for Regenerative Medicine Realization from the Ministry of Education, Science, Sports, Culture and Technology of Japan.

Send Correspondence to Dr. Takayuki Nakagawa, Department of Otolaryngology–Head and Neck Surgery, Graduate School of Medicine, Kyoto University, Kawaharacho 54, Shogoin, Sakyo-ku, 606-8507 Kyoto, Japan. E-mail: tnakagawa@ent.kuhp.kyoto-u.ac.jp

DOI: 10.1097/01.mlg.0000200791.77819.eb

MATERIALS AND METHODS

Experimental Animals

Sprague-Dawley rats (Japan SLC Inc., Hamamatsu, Japan) at 10 weeks of age were used as experimental animals. The Animal Research Committee of the Graduate School of Medicine, Kyoto University, Japan, approved all experimental protocols. Animal care was conducted under the supervision of the Institute of Laboratory Animals at the Graduate School of Medicine, Kyoto University. All experimental procedures were performed in accordance with the U.S. National Institutes of Health guidelines for the care and use of laboratory animals.

Preparation of Hydrogels

The biodegradable hydrogels were prepared as described previously.[8] Briefly, the gels were generated by the glutaraldehyde crosslinking of porcine type-I collagen (Gunze, Ayabe, Japan). The rates of degradation were determined according to the concentration of glutaraldehyde. The present study used a hydrogel that was made with 60 mol/L glutaraldehyde, which could release basic fibroblast growth factor[8] and BDNF[3] for 7 days in vivo.

Local Application of Insulin-Like Growth Factor-1

RhIGF-1 was provided by Astellas Pharma Inc., Tokyo, Japan. After measuring the auditory brain stem responses (ABRs), the otic bulla of the left temporal bone was exposed using a retroauricular approach under general anesthesia with ketamine (100 mg/kg intramuscularly [IM]; Sankyo Co., Tokyo, Japan) and xylazine (9 mg/kg IM; Bayer, Tokyo, Japan). A small hole was made on the left bulla to expose the round window niche. A hydrogel in dry condition was cut into the size of 2 mm^3 under the microscope and immersed with rhIGF-1 (400 μg dissolved in 40 μL physiological saline) 30 minutes before application. The hydrogel was then placed on the round window membrane (RWM) of the IGF group animals (n = 10). The animals applied a hydrogel-immersed physiological saline were used as controls (n = 10).

Noise Exposure and Measurement of Hearing

On day 3 after the IGF-1 application, we measured the ABRs to eliminate animals that showed threshold shifts of more than 10 dB at any frequencies from the experiments. In consequence, no animals showed threshold shifts over 10 dB after local drug application in the present study. The animals were then exposed to white noise at 120 dB sound pressure level (SPL) for 2 hours in a ventilated sound exposure chamber. The sound levels were monitored and calibrated at multiple locations within the sound chamber to ensure uniformity of the stimulus.

Auditory function was assessed by recording ABRs. The measurements of ABR thresholds were performed at frequencies of 8, 16, and 32 kHz before noise exposure and days 7 and 30 after noise exposure. Animals were anesthetized with ketamine (100 mg/kg) and xylazine (9 mg/kg) and kept warm with a heating pad. Generation of acoustic stimuli and subsequent recording of evoked potentials were performed using a PowerLab/4sp (AD Instruments, Castle Hill, Australia). Acoustic stimuli, consisting of tone-burst stimuli (0.1 ms cos^2 rise/fall and 1-ms plateau), were delivered monaurally through a speaker (ES1spc; Bioresearch Center, Nagoya, Japan) connected to a funnel fitted into the external auditory meatus. To record bioelectrical potentials, subdermal stainless steel needle electrodes were inserted at the vertex (ground), ventrolateral to the measured ear (active) and contralateral to the measured ear (reference). Stimuli were calibrated against a ¼-inch free-field microphone (ACO-7016; ACO Pacific, Inc., Belmont, CA) connected to an oscilloscope (DS-8812 DS-538; Iwatsu Electric, Tokyo, Japan) or a sound level meter (LA-5111; Ono Sokki, Yokohama, Japan). The responses between the vertex and mastoid subcutaneous electrodes were amplified with a digital amplifier (MA2; Tucker-Davis Technologies, Alachua, FL). Thresholds were determined from a set of responses at varying intensities with 5-dB SPL intervals and electrical signals were averaged for 1024 repetitions. Thresholds at each frequency were verified at least twice.

Histologic Analysis

On day 7 or 30 after noise exposure, five cochleae from each experimental group were provided for histologic analysis. The animals were anesthetized with ketamine and xylazine, and the left cochleae were exposed. After removal of otic vesicles, 4% paraformaldehyde in 0.01 mol/L phosphate-buffered saline (PBS)

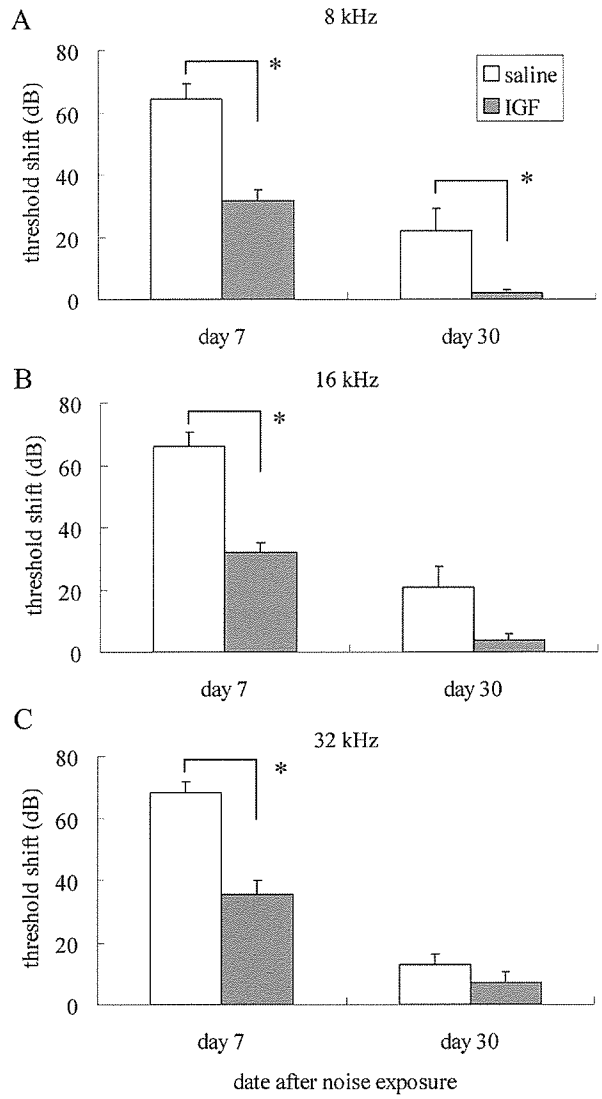

Fig. 1. Auditory brain response threshold shifts for recombinant human insulin-like growth factor-1- (rhIGF-1) and saline-treated cochleae at 8, 16, and 32 kHz on days 7 and 30 after noise exposure. An overall effect of local rhIGF-1 treatment is significant at 8, 16, or 32 kHz (two factorial analysis of variance). Asterisks are indicated significant differences in pairwise comparisons with Fisher's protected least-significant difference. Bars represent standard error (SE).

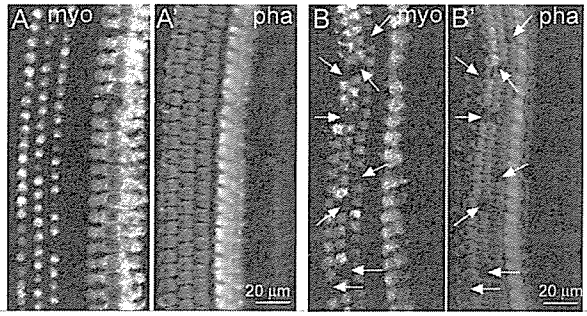

Fig. 2. Photomicrographs of surface preparations stained with myosin VIIa and phalloidin from the second turn of cochleae treated with recombinant human insulin-like growth factor-1 (**A**) or physiological saline (**B**) on day 30. Figures A and B show immunostaining for myosin VIIa (myo), and Figures A' and B' show F-actin labeling by phalloidin. Arrows indicate missing outer hair cells.

at pH 7.4 was gently introduced into the perilymphatic space of the cochleae. The temporal bones were then excised and immersed in the same fixative at 4°C for 12 hours. After rinses with PBS, the cochleae were dissected from the temporal bones and subjected to histologic analysis in whole mounts. We used three regions of cochlear sensory epithelia at a distance of 30% to 40% (apical), 50% to 60% (middle) or 80% to 90% (basal) from the apex for quantitative assessments of hair cell loss.

Immunohistochemistry for myosin VIIa and F-actin labeling by phalloidin were used to label the surviving inner hair cells (IHCs) and outer hair cells (OHCs). Anti-myosin VIIa rabbit polyclonal antibody (1:300; a gift from Tama Hasson, San Diego, CA) was used as the primary antibody, and Alexa-594-conjugated antirabbit goat IgG (1:400; Molecular Probe, Eugene, OR) was used as the secondary antibody. After immunostaining for myosin VIIa, specimens were stained with FITC-conjugated phalloidin (1:300; Molecular Probe). Specimens were viewed using a Leica TCS SP2 confocal microscope (Leica Microsystems Inc., Wetzlar, Germany). Nonspecific labeling was tested by omitting the primary antibody from the staining procedures. We counted the numbers of IHCs and OHCs in 0.2-mm long regions of the apical, middle, or basal portion of cochleae, respectively.

Statistical Analyses

An overall effect on ABR threshold shifts of application of rhIGF-1 was examined by the two-way factorial analysis of variance. When the interaction was significant, multiple comparisons with Fisher's protected least-significant difference (PLSD) were used for pairwise comparisons. The differences in OHC numbers in each region of the cochlea between the rhIGF-1- and saline-treated cochleae were examined using the Student t test. A P value less than .05 was considered statistically significant. Values are expressed as the mean ± standard error.

RESULTS

Functional Protection

The time course of alterations in ABR threshold shifts after noise exposure at 8, 16, or 32 kHz is shown in Figure 1. Local rhIGF-1 treatment demonstrated significant effects on ABR threshold shifts at each frequency. An overall effect on data for 8 kHz of rhIGF-1 application was significant ($P < .001$). The differences in threshold shifts between rhIGF-1- and saline-treated cochleae on days 7 and 30 were significant at multiple comparisons with Fisher's PLSD ($P < .001$ for day 7, $P = .039$ for day 30). An overall effect on data for 16 or 32 kHz of rhIGF-1 application was significant ($P < .001$ for 16 kHz, $P = .005$ for 32 kHz). The difference in threshold shifts at 16 kHz between rhIGF-1- and saline-treated cochleae was significant on day 7 ($P < .001$), but not on day 30 ($P = .051$). The difference in threshold shifts at 32 kHz between rhIGF-1- and saline-treated cochleae was significant on day 7 ($P < .001$), but not on day 30 ($P = .48$).

Histologic Protection

Immunostaining for myosin VIIa and phalloidin staining demonstrated degeneration of OHCs in the apical, middle, and basal portions of saline-treated cochleae (Fig. 2B), whereas OHC degeneration was very limited in rhIGF-1-treated cochleae (Fig. 2A). Conversely, IHC loss was not apparent in every region of both saline- and rhIGF-1-treated cochleae. Quantitative assessments revealed the significant differences in the degree of OHC loss between saline- and rhIGF-1-treated cochleae on days 7 and 30 (Fig. 3). The differences in the degree of OHC loss between the saline- and rhIGF-1-treated cochleae were significant in the apical ($P = .0006$), middle ($P < .0001$), and basal portion ($P = <.0001$) of cochleae on day 7, and in the apical ($P = .0006$), middle ($P < .0001$), and basal portion ($P = .002$) of cochleae on day 30. IHC loss was 2.7 ± 1.3% in the basal, 1.0 ± 0.5% in the middle, or 1.1 ± 0.8 in the apical portion of saline-treated cochleae, and 2.0 ±

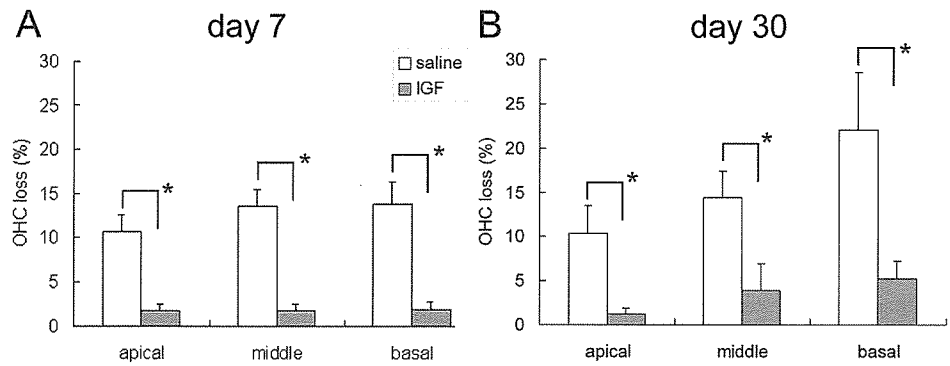

Fig. 3. Means of the percentage outer hair cell loss in the apical, middle, and basal portions of insulin-like growth factor-1- and saline-treated cochleae on days 7 (**A**) and 30 (**B**). Asterisks indicate significant differences with unpaired t test. Bars represent standard error (SE).

1.4% in the basal, 1.2 ± 0.9% in the middle, or 0.6 ± 0.6 in the apical portion of rhIGF-1-treated cochleae on day 30. No significant differences in the loss of IHCs were identified between the two experimental groups.

DISCUSSION

Our findings demonstrate that local rhIGF-1 application using a hydrogel before noise exposure has significant effects on reduction of ABR threshold shifts and of OHC loss. Our previous study has demonstrated the efficacy of local BDNF delivery to the cochlea by the biodegradable hydrogel.[3] The present findings therefore indicate that the biodegradable hydrogel can be used for local rhIGF-1 application to the cochlea. Our previous findings[3] demonstrate that high concentrations of BDNF in the cochlear fluid are maintained during days 3 to 7 after local BDNF application using this system. We then locally applied rhIGF-1 3 days before noise exposure to obtain sufficient concentrations of rhIGF-1 in the cochlear fluid. As expected, the pretreatment with rhIGF-1 demonstrated sufficient protective effects against noise trauma in the present study. However, in clinical settings, drug application after the onset of hearing loss is usually performed. Hence, we should examine the efficacy of local rhIGF-1 treatment after onset of hearing loss in the near future.

In the present study, we focused on degeneration of sensory hair cells in histologic analysis, because the degree of hair cell loss has traditionally been used to evaluate both the extent of noise-induced injury and the efficacy of protective treatments.[9,10] Quantitative assessments in the present study demonstrated significant protection of OHCs from noise trauma by local rhIGF-1 treatment. As for mechanisms of OHC protection by rhIGF-1, several possible explanations are aroused. One possible explanation is the rescue of OHCs from apoptosis resulting from noise by rhIGF-1. IGF-1 is known to inhibit apoptosis by downregulating the expression of proapoptotic genes,[11] and apoptosis is involved in OHC degeneration resulting from noise.[12] Another mechanism is the regulation of glucose transporters in OHCs by rhIGF-1. The expression of glucose transporter-5 (GLUT-5) in OHCs and its importance in their function have been reported.[13,14] GLUTs operate in the first step of glucose utilization by promoting the transport of glucose across the plasma membrane.[15] IGF-1 can regulate the expression of GLUT-5, thereby promoting neuronal cell survival.[16] Such mechanisms might be involved in the rhIGF-1-induced protection of OHCs against noise-induced injury. Further studies are required for elucidation of detailed mechanisms for the rhIGF-1-induced protection of OHCs.

ABR threshold shifts observed on day 7 remarkably recovered on day 30, whereas the damage in the organ of Corti moderately progressed until day 30. This indicates that ABR threshold shifts observed on day 7 may be caused not only by the damage in the organ of Corti, but also by reversible damages in other regions of the cochlea. In addition, the damage in the organ of Corti on day 7, 10% to 14% loss of OHCs and limited loss of IHCs, is not compatible with over 60 dB ABR threshold shifts. Recent studies have indicated involvement of damages in the cochlear lateral wall in noise-induced HL.[17] Local rhIGF-1 treatment significantly reduced ABR threshold shifts on day 7. IGF-1 has also effects on promotion of survival of fibloblasts.[18] Therefore, protective effects of IGF-1 on the fibrocytes in the spiral ligament may be involved in mechanisms for significant reduction of ABR threshold shifts on day 7.

CONCLUSION

This report demonstrates the efficacy of local rhIGF-1 application using a biodegradable hydrogel for the protection of cochleae from noise-induced hearing loss. Because the materials used in the present study are suitable for clinical application, the present findings encourage us to conduct further studies for clinical application of local rhIGF-1 treatment using the biodegradable hydrogel. However, the exact mechanisms by which rhIGF-1 acts in the cochlea are presently unclear and require further research. Furthermore, rhIGF-1 was applied before the onset of noise-induced hearing loss in the present study. The ability of rhIGF-1 to ameliorate cochlear damages when applied locally after the onset of hearing loss should therefore be examined in an experimental model in the near future.

Acknowledgments

The authors thank T. Hasson for providing the antibody for myosin VIIa.

BIBLIOGRAPHY

1. Arnold W, Senn P, Hennig M, et al. Novel slow- and fast-type drug release round-window microimplants for local drug application to the cochlea: an experimental study in guinea pigs. *Audiol Neurotol* 2005;10:53–63.
2. Tamura T, Kita T, Nakagawa T, et al. Drug delivery to the cochlea using PLGA nanoparticles. *Laryngoscope* 2005; 115:2000–2005.
3. Endo T, Nakagawa T, Kita T, et al. A novel strategy for treatment of inner ears using a biodegradable gel. *Laryngoscope* 2005;115:2016–2020.
4. Varela-Nieto I, Morales-Garcia JA, Vigil P, et al. Trophic effects of insulin-like growth factor-I (IGF-I) in the inner ear. *Hear Res* 2004;196:19–25.
5. Linseman DA, Phelps RA, Bouchard RJ, et al. Insulin-like growth factor-I blocks Bcl-2 interacting mediator of cell death (Bim) induction and intrinsic death signaling in cerebellar granule neurons. *J Neurosci* 2002;22: 9287–9297.
6. Staecker H, Van De Water TR. Factors controlling hair-cell regeneration/repair in the inner ear. *Curr Opin Neurobiol* 1998;8:480–487.
7. Malgrange B, Rigo JM, Coucke P, et al. Identification of factors that maintain mammalian outer hair cells in adult organ of Corti explants. *Hear Res* 2002;170:48–58.
8. Iwakura A, Fujita M, Kataoka K, et al. Intramyocardial sustained delivery of basic fibroblast growth factor improves angiogenesis and ventricular function in a rat infarct model. *Heart Vessels* 2003;18:93–99.
9. Keithley EM, Ma CL, Ryan AF, et al. GDNF protects the cochlea against noise damage. *Neuroreport* 1998;9: 2183–2187.
10. Shoji F, Miller AL, Mitchell A, et al. Differential protective effects of neurotrophins in the attenuation of noise-induced hearing loss. *Hear Res* 2000;146:132–142.
11. Linseman DA, Phelps RA, Bouchard RJ, et al. Insulin-like growth factor-I blocks Bcl-2 interacting mediator of cell

death (Bim) induction and intrinsic death signaling in cerebellar granule neurons. *J Neurosci* 2002;22: 9287–9297.
12. Pirvola U, Xing-Qun L, Virkkala J, et al. Rescue of hearing, auditory hair cells, and neurons by CEP-1347/KT7515, an inhibitor of c-Jun N-terminal kinase activation. *J Neurosci* 2000;20:43–50.
13. Nakazawa K, Spicer SS, Schulte BA. Postnatal expression of the facilitated glucose transporter, GLUT 5, in gerbil outer hair cells. *Hear Res* 1995;82:93–99.
14. Belyantseva IA, Adler HJ, Curi R, et al. Expression and localization of prestin and the sugar transporter GLUT-5 during development of electromotility in cochlear outer hair cells. *J Neurosci* 2000;20:RC116.
15. Bell GI, Kayano T, Buse JB, et al. Molecular biology of mammalian glucose transporters. *Diabetes Care* 1990;13: 198–208.
16. Asada T, Takakura S, Ogawa T, et al. Overexpression of glucose transporter protein 5 in sciatic nerve of streptozotocin-induced diabetic rats. *Neurosci Lett* 1998; 252:111–114.
17. Hirose K, Liberman MC. Lateral wall histopathology and endocochlear potential in the noise-damaged mouse cochlea. *J Assoc Res Otolaryngol* 2003;4:339–352.
18. Heron-Milhavet L, Karas M, Goldsmith CM, et al. Insulin-like growth factor-I receptor activation rescues UV-damaged cells through a p38 signaling pathway. *J Biol Chem* 2001;276:18185–18192.

Journal of
Nanoscience and Nanotechnology
Vol. 7, 763–772, 2007

RESEARCH ARTICLE

Effect of Pore Size of Self-Organized Honeycomb-Patterned Polymer Films on Spreading, Focal Adhesion, Proliferation, and Function of Endothelial Cells

Masaru Tanaka[1,2,*,†], Aiko Takayama[2], Emiko Ito[2], Hiroshi Sunami[1,2], Sadaaki Yamamoto[1,2], and Masatsugu Shimomura[2,3]

[1] *Creative Research Initiative "Sousei", Hokkaido University, Kita-Ku N21W10, Sapporo 001-0021, Japan*
[2] *CREST, Japan Science and Technology Corporation, Honchou 4-1-8, Kawaguchi 332-0012, Japan*
[3] *Nanotechnology Research Center, Research Institute for Electronic Science, Hokkaido University, Kita-Ku N21W10, Sapporo 001-0021, Japan*

The design of nano- and microstructures based on self-organization is a key area of research in the search for new materials, and it has a variety of potential applications in tissue engineering scaffolds. We have reported a honeycomb-patterned polymer film (honeycomb film) with highly regular pores that is formed by self-organization. This study describes the behavior of vascular endothelial cells (ECs) on honeycomb films with four different pore sizes (5, 9, 12, and 16 μm) as well as on a flat film. We examined the influence of the honeycomb pattern and pore size on cell behavior. The changes in cell morphologies, actin filaments, vinculin clusters, cell proliferation, and secreted extracellular matrix (ECM) (fibronectin, laminin, type IV collagen, and elastin) production profiles were observed by using optical, fluorescence, and scanning electron microscopy. The ECs that adhered to the flat film showed an elongated morphology with random orientation; the actin filaments and focal adhesions were not conspicuous. On the other hand, the ECs on the honeycomb films exhibited greater spreading and flattening; the degree of spreading of the ECs increased with an increase in the pore size. The actin filaments and focal adhesions appeared conspicuous, and the focal adhesions localized along the edge of the honeycomb pores were distributed over the entire projected cell area. The honeycomb film with a pore size of 5 μm showed the highest cell proliferation and ECM production profiles. These results suggest that the honeycomb film is a suitable material for designing a new vascular device.

Keywords: Cell Adhesion, Self-Organization, Scaffold, Pore Size, Focal Adhesion.

1. INTRODUCTION

Porous scaffolds fabricated from biodegradable polymers have been widely used as temporary extracellular matrices (ECMs) and play critical roles in tissue engineering and *in situ* tissue reconstruction.[1–4] Scaffolds with appropriate porosities and interconnected pores are required to facilitate cell adhesion, ECM secretion, and eventual tissue regeneration. A number of fabrication methods, including phase separation and lithography techniques, have been developed and applied to the fabrication of porous scaffolds from biodegradable polymers.[5–11] These techniques are certainly useful in the fabrication of porous scaffolds. However, these techniques require a large amount of energy and involve many processes. In addition, a limited variety of materials is available for scaffolds. Each of these approaches is very different and has a unique set of characteristics that have some limitations, including uncontrolled pore size and size distribution. As a result, there is a high demand for suitable alternative methods for preparing scaffolds. Inspired by biology, the self-organization of organic and inorganic components into hierarchical and sophisticated structures offers an alternative to the conventional techniques of nano- and microfabrication. The process occurs under ambient physiological conditions in contrast to typical fabrication techniques that

*Author to whom correspondence should be addressed.
†Present address: Nanotechnology Research Center, Research Institute for Electronic Science, Hokkaido University, Kita-Ku N21W10, Sapporo 001-0021, Japan

require harsh conditions. It can be applied to polymer fabrication because of its physical generality. We have found that typical regular structures are formed during the process of casting of polymer solutions on solid surfaces; for example, self-organized honeycomb-patterned polymer films (honeycomb films) with highly regular porous structures can be prepared under humid casting conditions.[12–24] The pore size can be controlled in the range of 100 nm to 50 μm by changing the casting conditions. This method has a great advantage in that the films can be prepared with ease, at a low cost, and without any limitations pertaining to the availability of materials for the scaffold. The process is relatively easy to scale up and is being used for the commercial production of porous scaffolds.

The impact of the surface topography of a polymer on cell adhesion was a matter of concern because the nano- and microscale pattern of a surface can exert a significant effect on the adhesion behavior of cells on the surface.[25–27] In particular, the pore size of a tissue engineering scaffold could influence cell adhesion and subsequently, their proliferation. One of the keys in vascular tissue engineering and bioartificial vessel development is the design of a porous polymer scaffold of effective pore size for facilitating the adhesion and functions of vascular endothelial cells (ECs).[28] However, it is difficult to control the adhesion of these cells and enhance their functions *in vitro*. Additionally, EC activities are often limited by the lack of an EC-specific environment.

Here, we describe the fabrication of honeycomb films by using a solution casting technique under humid air conditions. Additionally, we also examined a culture of ECs on these films in order to investigate the influence of the honeycomb pattern and the pore size on cell morphologies, actin filaments, vinculin clusters, proliferation, and secreted ECM (fibronectin, laminin, type IV collagen, and elastin) production profiles. These regular arrays of pores allowed the specific interactions of the cells. The influence of pore size on cell adhesion and proliferation or function may provide valuable information for designing appropriate polymer scaffolds used in vascular tissue engineering.

2. EXPERIMENTAL DETAILS

2.1. Materials

Honeycomb films were fabricated using biodegradable polymers poly(ε-caprolactone) (PCL; MW = 70,000–100,000; Fig. 1(a)) and a copolymer of dodecylacrylamide and ω-carboxyhexylacrylamide (Cap; MW = 22,000; Fig. 1(b)). Cap was used as an emulsifier in this study. The copolymer was synthesized by using a previously reported method.[29] The copolymer is amphiphilic because the polymer forms a stable monolayer at the air–water interface. The water was purified by a Millipore system (Milli-Q, Millipore). Organic solvents and other

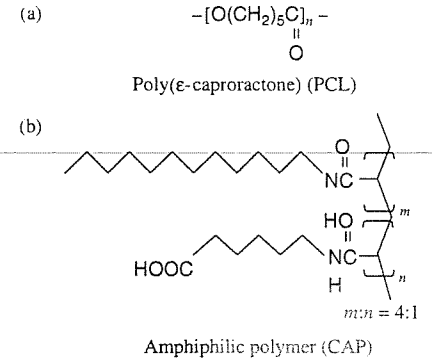

Fig. 1. Chemical structures of (a) poly(ε-caprolactone) (PCL) and (b) copolymer of dodecylacrylamide and ω-carboxyhexylacrylamide (Cap).

chemicals were commercially available and were used without further purification.

2.2. Preparation of Honeycomb and Flat Films

The honeycomb film was prepared on a glass substrate by employing a previously described method.[15–23] In brief, PCL and Cap (10:1 wt%) were dissolved in chloroform at a concentration of 5 g/L. The polymer solution was poured into a round glass dish (9.3 cm in diameter) with blowing of highly humid air (1.0 L/min). The flat film was prepared as follows. The PCL and Cap solution (5 g/L) was poured onto a glass slide. The cover glass with the polymer layer was spun at 1000 rpm for 30 s using a spin coater (1H-7D, Mikasa). These films were immersed in 1-propanol for 12 min to remove Cap. The static contact angle of the films was measured at room temperature (23 °C–25 °C) by sessile drop method using a contact angle goniometer (Face CA-A, Kyowa Interface Science).

2.3. Culturing of ECs

Porcine aortic ECs (CSC Certificate™ Dainippon Pharmaceutical) were purchased. The frozen cells were thawed at 37 °C and then resuspended in a culture medium (Dulbecco's Modified Eagle's Minimal Essential Medium, Sigma). Subsequently, 10% fetal bovine serum (FBS), 100 unit/ml penicillin, and 100 μg/ml penicillin-streptomycin (Gibco) were added. A honeycomb film and a flat film on a glass plate were preincubated in a culture medium for 72 h at 37 °C in 5% CO_2 before cell seeding. The ECs were seeded on the films at a density of 1.5×10^4 cells/cm^2. The ECs at passages 6–8 were used in the experiments. In preliminary experiments, we established that the differences in passage number did not affect the outcome of our study. The culture medium was replaced after days 1, 3, 5, and 7 without damaging the films. The morphologies of the ECs after seeding were observed under a phase contrast microscope (IX 70, Olympus) until the ECs proliferated to confluence. After 1 to 9 days of

culture, the number of ECs on each film was evaluated with the cell proliferation reagent WST-1 (F. Hoffmann-La Roche).

2.4. Scanning Electron Microscopic Observation

The ECs that were cultured 1 to 9 days after seeding were fixed in 2% glutaraldehyde in phosphate-buffered saline (PBS; Wako) and were incubated over night at 4 °C. After washing three times with PBS, each sample was fixed in 1.0% osmium tetroxide (Wako) aqueous solution for 1 h and was rinsed in PBS. Subsequently, the samples were dehydrated by washing in increasing concentrations of ethanol and were then air dried. The samples were transferred to microporous specimen capsules and dried by means of a critical point dryer (HCP-2, Hitachi). The dried samples were mounted on aluminum stages by using double-stick tape, and they were coated with palladium gold (approximately 5 nm of coating) by using an ion sputter coater (E-1030, Hitachi). All samples were observed using a scanning electron microscope (SEM; S-3500N, Hitachi).

2.5. Actin, Vinculin, and ECM Staining by Confocal Laser Scanning Microscopy

The actin filaments in the ECs that were cultured 5 days after seeding were stained. After washing with PBS, the cells were fixed with 10% formaldehyde (Wako) for 30 min at 22 °C. The cells were washed twice with PBS and permeated with 1% Triton X-100 in PBS solution for 5 min at 22 °C and 1.0% bovine serum albumin (Sigma) in PBS. To visualize the cytoskeletal element actin fiber, focal adhesion vinculin, and ECM (fibronectin, laminin, type IV collagen, and elastin) production profiles, staining was performed by an immunological method using primary antibodies (diluted 1:100, Chemicon) for each antigen and fluorescence-labeled secondary antibodies (diluted 1:1000; Alexa Fluor 546 goat anti-mouse IgG or Alexa Fluor 488 phalloidin, Molecular Probes). The stained cells were rinsed four times with PBS, and subsequently immersed for 1 h at the fourth rinse. All samples were applied to slides. Coverslips were placed on the samples and sealed with nail polish. A confocal laser scanning microscope (CLSM; FV-300, Olympus) was used for observation. The projected areas and the number of focal adhesions of isolated cells on the film were analyzed with an NIH image software.

3. RESULTS AND DISCUSSION

3.1. Honeycomb Film

The SEM showed a highly regular hexagonal arrangement of pores (honeycomb-patterned structure), and a well

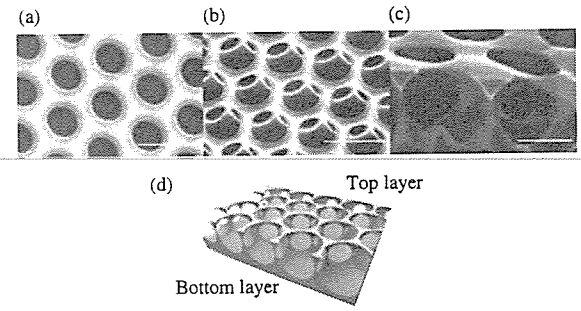

Fig. 2. SEM images of the honeycomb film (a) surface, (b) tilted, and (c) cross section. (d) Schematic representation of the 3-D structure of the honeycomb film. The pore structure (spherical shape) reflects the use of water droplet as a template.

interconnected, uniform pore structure (pore size: approximately 5 μm; Figs. 2(a–c)). The 3-D structure could affect the flow of nutrients and wastes. A schematic cross section of this regular microporous film is shown in Figure 2(d). Condensation due to the evaporation cooling of humid air occurred when a water-immiscible solvent was used. Self-packed and mono-dispersed water droplets that formed on the solution surface act as a temporary template for pores. In general, the condensed water droplets are not stable and eventually start coalescing. In order to prepare a highly regular porous (honeycomb-patterned) film, the stabilization of the water droplets is necessary. The role of the amphiphilic polymer in pattern formation is to prevent the fusion of the water droplets. Cap (Fig. 1(a)) acts as a surfactant and contributes to the stabilization of the water droplets at the interface of the polymer solution and water. As a result, the fusion of the water droplets is prevented due to the intervening amphiphilic polymer layer. Most polymers dissolved in a water-immiscible solvent can be fabricated to a honeycomb film by the addition of Cap. Various experimental factors affected the pore structures. A uniform pore size can be achieved by changing the casting conditions.[12–23] In this study, honeycomb films with four different pore sizes, 5, 9, 12, and 16 μm, that were narrower than the diameter of an EC in suspension were prepared by changing the casting volume (Fig. 3 and Table I). The rim of the honeycomb films widened with an increase in the pore size. The length of pore edge per unit surface area is greatest in the smaller pore size. The porosity of each film was approximately 50%. The contact angles of the honeycomb films were approximately 105° regardless the pore size. This indicates an increase in the hydrophilicity when compared with a flat film with a contact angle of 74°. Unlike other template or lithographic methods, the advantage of this method is the ease with which patterned surfaces can be fabricated using various materials without the consumption of a large amount of energy. In this study, PCL was selected as the matrix polymer due to its highly pliable nature.

RESEARCH ARTICLE

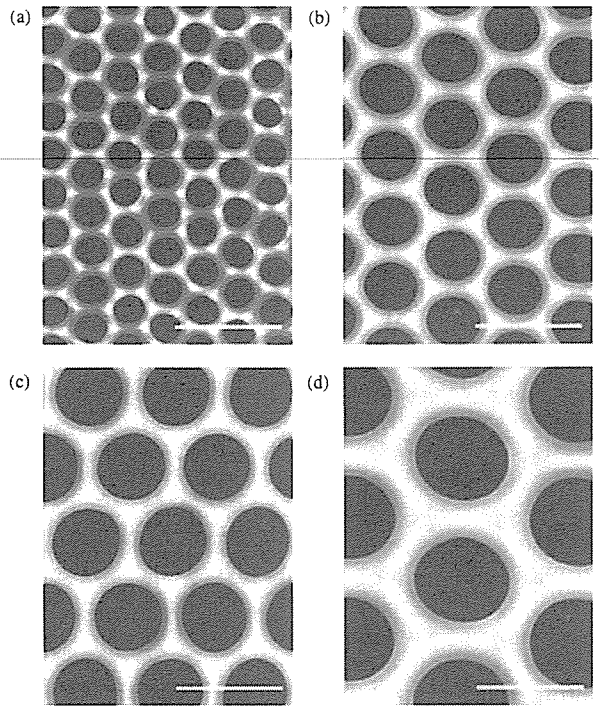

Fig. 3. SEM images of the honeycomb films. The pore sizes were approximately (a) 5 μm, (b) 9 μm, (c) 12 μm, and (d) 16 μm. Bar: 20 μm.

3.2. Morphologies of Adhered ECs on Honeycomb and Flat Films

Most tissue-derived cells are anchorage dependent and require attachment to a solid surface for viability and growth. For this reason, the initial events that occur when a cell approaches a surface are of fundamental interest. In tissue engineering, cell adhesion to a surface is critical because adhesion precedes other events, such as cell spreading, cell migration, and differentiated cell functions. The ability of the honeycomb film to support an EC culture was investigated *in vitro*. The adhesion and proliferation behavior of the ECs and their morphology on the honeycomb films were characterized on the basis of SEM observation. Figure 4 shows the morphology of ECs adhering on the films after 5 days of incubation. The morphology of the ECs on the honeycomb film was compared with that of those on the flat film. Different EC morphologies were observed on both the films. The ECs on the flat film showed an elongated morphology with random orientation (Figs. 4(a, d)). The flat film restricted cell spreading but did not inhibit cell adhesion. The ECs attached to the honeycomb films exhibited greater cell spreading and flattening. Small protrusions were observed around the ECs. The ECs were well spread along the honeycomb rims; this was maintained at least until the cells reached near confluence. This behavior is expected to exhibit better and prolonged EC function. Several parameters have been used to describe cell shape and spreading.[30] For comparison, the cell projected area was used to quantify the morphological response of cells that showed spreading on the films. The average EC projected area on the flat film was approximately 2,500 μm^2 and that on the honeycomb films was approximately 4,200 $\mu m.^2$ These results showed that greater cell adhesion could be achieved on a honeycomb film compared to a flat film. The honeycomb film has an adhesive property since the monolayer was appeared on the surface with the adhesive property. The cells could adhere and spread along the honeycomb pattern, but they did not extend into the pores of the honeycomb film via cell protrusions. Significant differences in the cell shape were found depending on the pore size of the honeycomb films. The degree of spreading of the ECs was enhanced with an increase in the pore size. It was observed that the thickness of the cells on the honeycomb film with 5 μm pores (Figs. 4(b, e)) was higher than that of those on the honeycomb film with 16 μm pores (Figs. 4(c, f)). This showed that the cells prefer to spread on a honeycomb film with a large pore size. It should be noted that both the flat and honeycomb films were prepared from the same polymer. This implies that the topological property of the honeycomb film affected the EC morphology. The honeycomb film may be appropriate for regulating the degree of cell–cell and cell–material interactions. The honeycomb pattern variations may also affect EC-specific functions. Further investigation is required for elucidating the mechanism of the interaction between ECs and the honeycomb film. However, the strategy of immobilization and stabilization of ECs through the use of honeycomb films would prove advantageous in designing a bioartificial vascular device, wherein the ECs could attach to a film with a high surface area, maintain their functions, and remain stable against the perfusion and shear forces in the blood vessel.

Table I. Properties of honeycomb and flat films.

	Flat film	Honeycomb films			
Pore size (μm)	—	5.3 (±0.02)	9.1 (±0.03)	11.8 (±0.15)	15.6 (±0.08)
Rim size (μm)	—	1.8 (±0.06)	3.1 (±0.20)	3.6 (±0.35)	7.1 (±0.15)
Poro edge length (μm)*	—	258.7 (±2.32)	187.9 (±2.81)	162.0 (±4.15)	87.3 (±2.73)
Porosity (%)	—	50.6 (±0.73)	51.0 (±1.65)	54.7 (±3.60)	42.6 (±13.63)
Contact angle (°)	73.9 (±1.45)	105.6 (±1.64)	104.3 (±3.73)	107.2 (±1.48)	105.0 (±3.86)

*The length of pore edge per unit surface area ($\times 10^3$ μm^2).

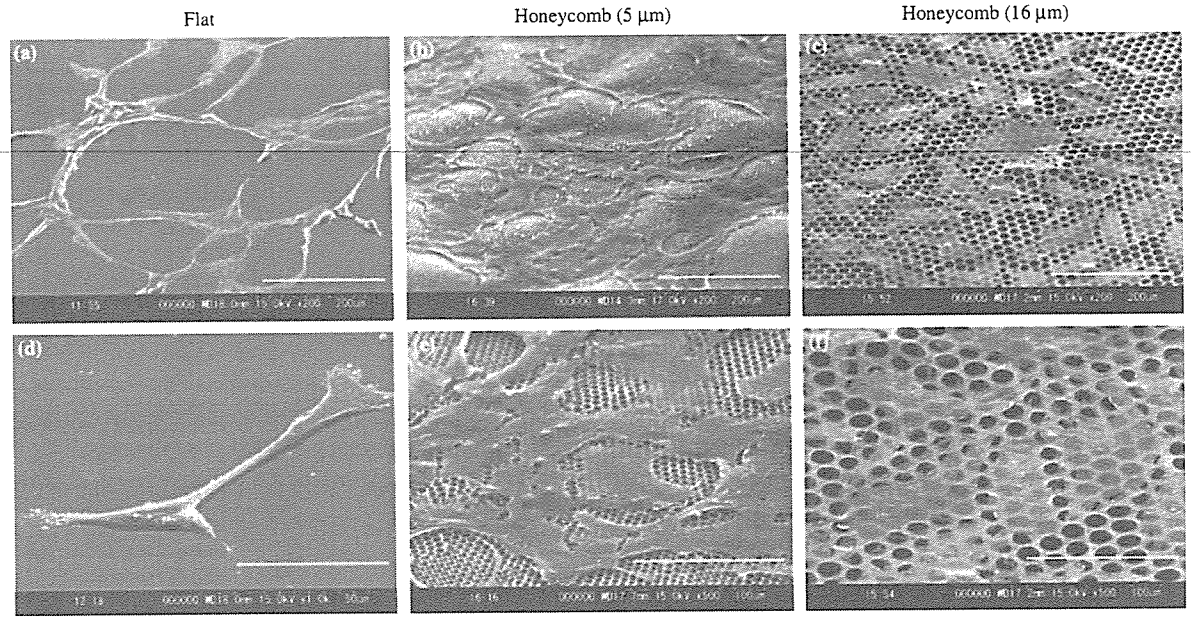

Fig. 4. SEM images of ECs cultured on the flat and honeycomb films. (a), (d): Cultured on the flat film for 5 days. (b), (e): Cultured on the honeycomb film (pore size, approximately 5 μm) for 5 days. (c), (f): Cultured on the honeycomb film (pore size, approximately 16 μm) for 3 days. Bar: (a), (b), (c) 200 μm; (d) 50 μm; (e), (f) 100 μm.

3.3. Proliferation Behavior of ECs on Honeycomb Films with Different Pore Sizes

Cell adhesion is a key step that occurs before cell proliferation. The variation in the cell adhesion may influence the cell proliferation. Figure 5 shows the proliferation profiles of ECs cultured on the honeycomb films. The number of ECs on the honeycomb film was compared with that of those on the flat film. The cell number tended to increase with incubation time, irrespective of the pore size of the honeycomb film. The honeycomb film with a pore size of 5 μm showed the highest proliferation. The number of cells on the honeycomb films was nearly two times that on the flat films. The proliferation increased with time for the initial 5 days and was saturated on day 7. The initial rate of cells grown was higher for the honeycomb films with 24 h culture, but once the cells reached confluent, the proliferation stopped. Figure 6 shows the SEM images of ECs on honeycomb films with different pore sizes. After 7 days of culture, the ECs were well spread and were able to form a confluent monolayer on the honeycomb film with a pore size of 5 μm.

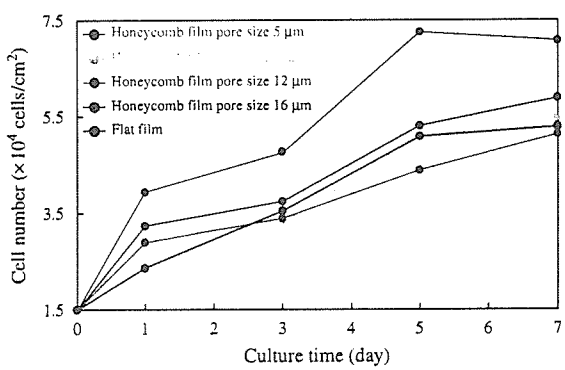

Fig. 5. Proliferation of the cultured ECs on the flat and honeycomb films.

The proliferation of cells on a scaffold requires oxygen and nutrient supply. The scaffold materials should provide such an environment for cells. The results of the cell adhesion and proliferation profiles (Figs. 5 and 6) revealed that diffusion of nutrients, bioactive factors, and oxygen and the exchange of wastes from the cells that was facilitated through these highly interconnected pores was sufficient for the survival of a large number of cells for extended periods of time. The honeycomb film may not only provide mechanical support for cells but also serve as a medium through which diffusion of soluble factors can occur. If the honeycomb film can promote the adhesion and growth of cells on its surface, it could have important biomedical applications.

3.4. Actin Filaments and Focal Adhesions

To clarify the reason for the greater cell proliferation on the 5 μm pore sized honeycomb film compared to the other films, the direct effect of the honeycomb films on the spatial arrangement of the cytoskeleton as well as on focal adhesion was investigated. Cytoskeletal actin is known as a liner protein that determines cell shape. In addition, it is also important in cellular functions and proliferation.

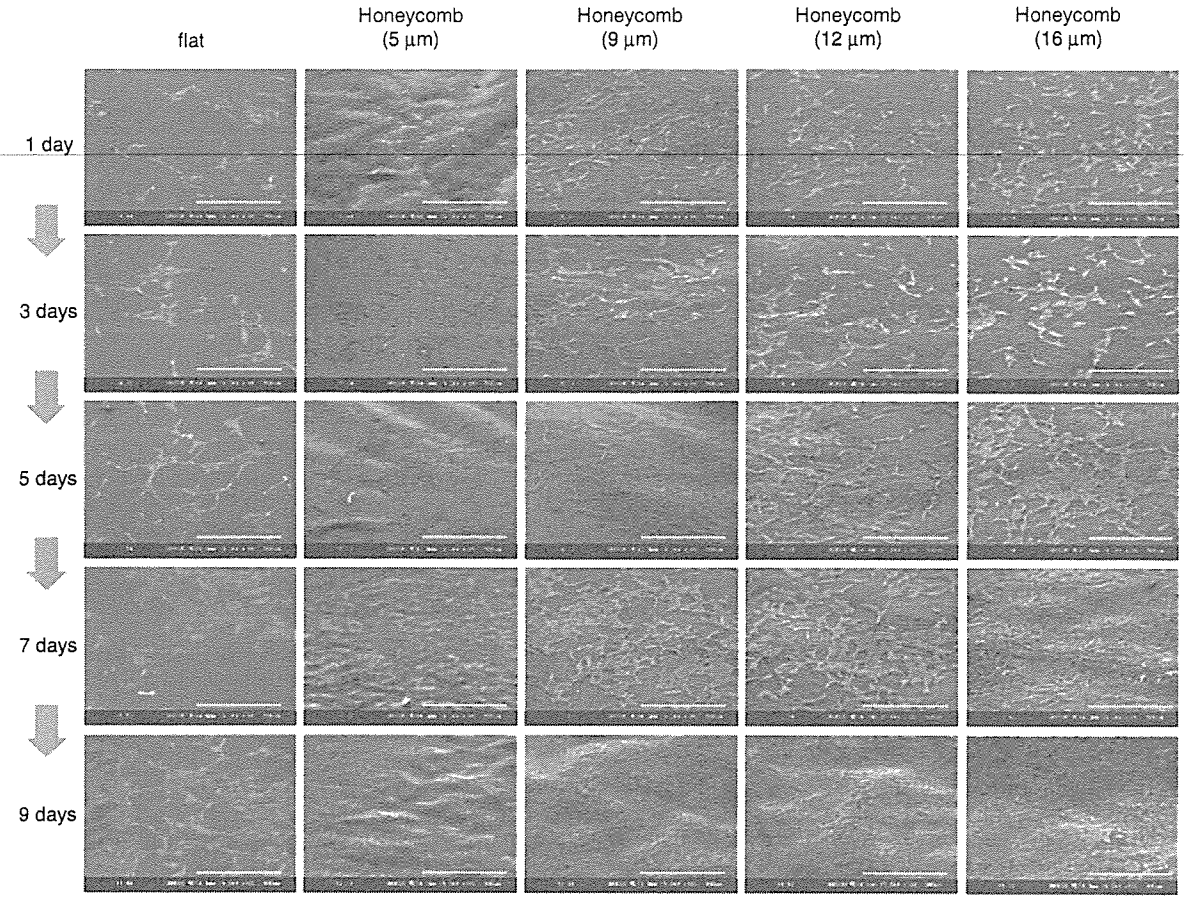

Fig. 6. SEM images of the ECs cultured on the flat and honeycomb films. Bar: 500 μm.

These events involve the development of specific intercellular adhesions and redistribution of cell–cell and cell–material adhesion forces that are intimately related to the dynamic cytoskeletal organization. Figures 7(a–c) shows the CLSM images of the actin filaments in the ECs adhered to both the flat and honeycomb films. The actin filaments were clearly observed in the spreading regions of the ECs on the honeycomb film (Figs. 7(b, c)). However, the actin filaments could not be clearly observed on the flat film (Fig. 7(a)). These results indicated that the honeycomb film could control EC adhesion following cytoskeletal protein production.

The cell proliferation is highly regulated by cell adhesion onto biomaterials. Focal adhesion proteins such as vinculin play a crucial role in cell-adhesion behavior and are major cellular sites responsible for cell–protein attachment. The morphology of focal adhesion was clearly different in the honeycomb film (Figs. 7(h, i)) and the flat film (Fig. 7(g)). The analysis of the confocal microscopy images showed that the focal adhesions could not be formed properly on the flat film (Fig. 7(g)). The focal adhesions existed locally at the intracellular edge of the elongated cells on the flat film. In contrast, the focal adhesions were localized along the edge of the honeycomb pores that were distributed over the entire projected cell area (Figs. 7(h, i)). The distribution of focal contacts along the pore edges suggests that strong adhesion sites were formed on the honeycomb film; however the flat film showed weak focal contacts. The honeycomb film with a pore size of 5 μm showed the highest number of focal adhesions due to a combination of the greater pore numbers and the length of pore edge per unit surface area. This implies that a higher focal adhesion density may induce a complex signal transduction for the proliferation of ECs. The site-selective distribution of focal adhesions indicates that ECs adhere to adsorbed proteins on the honeycomb rims. It was suggested that the difference in the cell proliferation properties of these films is caused by the difference in focal adhesions. In our experiments, the stained focal adhesion sites that existed at the intracellular edge were found to be composed of actin joined together with vinculin (Figs. 7(d–f)).

The results are of interest with regard to the Rho family of small GTPase. The Rho family has emerged as the key regulator of the actin cytoskeleton and it coordinates cellular activities, such as gene transcription and adhesion.[31]

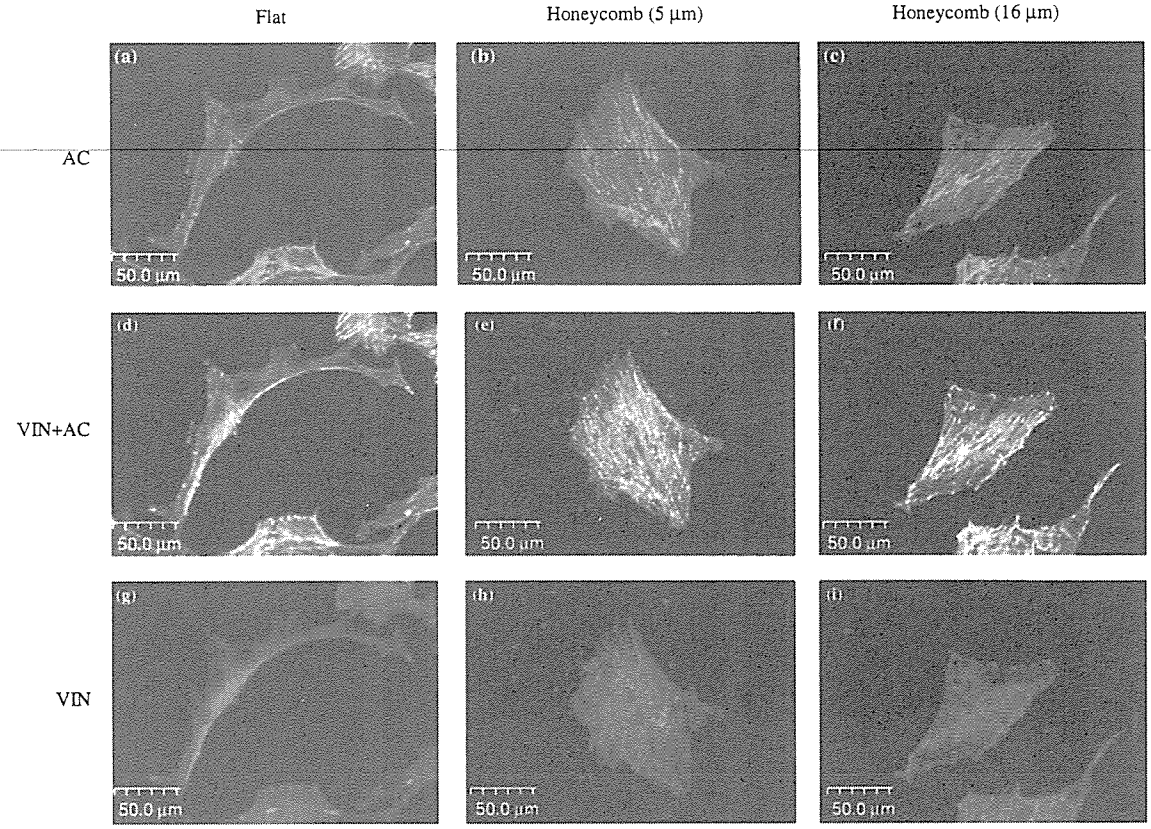

Fig. 7. CLSM images of ECs cultured on flat and honeycomb films. The cytoskeletal protein actin filaments and vinculin are stained using immunofluorescence. (a), (b), (c): Actin filaments. (d), (e), (f): Actin filaments and vinculin. (g), (h), (i): Vinculin. (a), (d), (g): Cultured on the flat film for 3 days. (b), (e), (h): Cultured on the honeycomb film (pore size, approximately 5 μm) for 3 days. (c), (f), (i): Cultured on the honeycomb film (pore size, approximately 16 μm) for 3 days. Bar: 50 μm.

It is possible that the topological properties of the honeycomb film affected the signal transduction involving the Rho family since morphology, actin localization, and focal adhesions of ECs on the honeycomb film were different from those on the flat film.

3.5. ECM Production

The EC morphology, formation of actin filaments, and focal adhesions are important factors that affect the EC function. The secretion of ECM is one of the EC-specific functions; therefore, we investigated the secreted ECM profiles. Figure 8 shows the data on ECM (fibronectin, laminin, type IV collagen, and elastin) production profiles 5 days after culture on both the flat and honeycomb films. The ECM production level in the cultured ECs on the honeycomb film was relatively high compared to that of those on the flat film. Collagen IV formed a dense fibrillar network on the honeycomb films with a pore size of 5 μm. This indicates that the cells exhibited more specific functions compared with those of the cells on the flat film. As mentioned above, the result indicated that ECM production reflected the morphology of the ECs since the relationship between morphology and functions was known. It was believed that the ECs on the honeycomb film tended to form tissue-like structures, and therefore, a high expression of ECM was observed. These results suggest that the honeycomb film may allow the enhancement and maintenance of EC function for a long period of time.

It is only recently that systematic studies involving surface chemistry and topography have received significant attention.[4, 25–27, 30] To date, topographic features have been shown to incite changes in the morphology of adherent cells. Several hypotheses regarding the mechanism of cellular reaction to topographical features have been proposed based on the geometrical details of the features that the cells may encounter. It is clear that the major cellular components responsible for these observations include actin filaments, focal adhesions, and outside to inside signal transducers such as integrins.[32–37] The topographic features also affect gene expression and protein synthesis and may influence other parts of the cellular machinery. However, the mechanism of the topological effect on cell behavior is still not well understood.

We found that the honeycomb film considerably affected not only cell adhesion but also proliferation and ECM

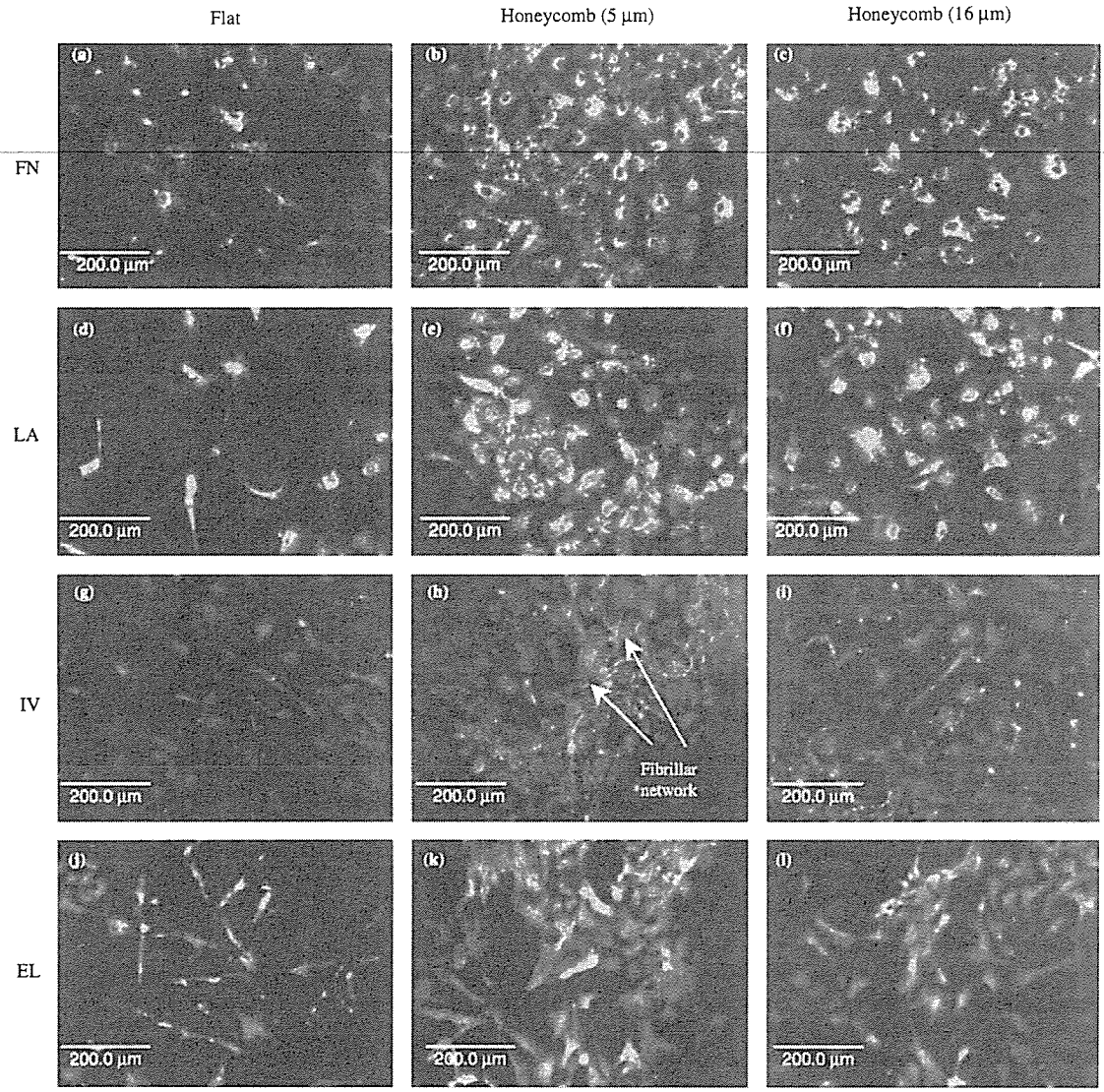

Fig. 8. CLSM images of ECs cultured on the flat and honeycomb films. Fibronectin, laminin, type IV collagen, and elastin are stained using immunofluorescence. (a), (b), (c): Fibronectin. (d), (e), (f): laminin. (g), (h), (i): Type IV collagen. (j), (k), (l): Elastin. Bar: 200 μm.

production of the ECs following actin and vinculin organization. These results indicate that the physical properties of films should be considered in the cases where porous films are used as scaffolds. The relationships between cell adhesion, cytoskeletal elements, focal adhesions, cell functions, and the dimensions of surface pattern are not fully understood. To date, there is little information regarding porous film-induced topological effects on ECs, although an optimal balance between the degree of cell–cell and cell–material interactions has been recognized as a critical factor for guiding three-dimensional cellular organization and improving EC functions on porous films used as tissue engineering scaffolds. The honeycomb film is also a useful tool for obtaining insights into the mechanism of cell–cell and cell–material interactions, which is one of the central research topics in tissue engineering.

At present, the mechanism by which the cells recognize the honeycomb film in cultures is unclear. It is generally known that the adhesion and morphology of cells are influenced by the variety and structure of proteins adsorbed on the material surface.[38] We have reported the adsorbed proteins and water on polymers in order to clarify the main factor that causes cell–material and protein–material interactions.[39,40] We have also reported that fibronectin that is site-selectively adsorbed onto the honeycomb film plays vital roles in cell adhesion, focal adhesion, and proliferation. It was demonstrated that the honeycomb film influenced cell behavior via the site-selectively adsorbed fibronectin molecules.[41,42] This type